Chemical Engineering Journal 493 (2024) 152514

Contents lists available at ScienceDirect

Chemical Engineering Journal

journal homepage: www.elsevier.com/locate/cej

# Nanoscale assembly of $MoS_2/CoS_2/Ni_3S_2$ grown on Ni foam for synergistic capture of iodine

Chaonan Wang [a], Huiqin Yao [b,*], Jingtong Sun [a,1], Tian Tong [a], Zi Ye [c], Hongliang Dong [c,d,*], Cheng Li [e,*], Shulan Ma [a,*]

[a] Beijing Key Laboratory of Energy Conversion and Storage Materials, College of Chemistry, Beijing Normal University, Beijing 100875, China
[b] School of Basic Medical Sciences, Ningxia Medical University, Yinchuan 750004, China
[c] Center for High Pressure Science and Technology Advanced Research, Pudong, Shanghai 201203, China
[d] Shanghai Key Laboratory of Material Frontiers Research in Extreme Environments (MFree), Shanghai Advanced Research in Physical Sciences (SHARPS), Pudong, Shanghai 201203, China
[e] Shanghai Institute of Applied Physics, Chinese Academy of Sciences, Shanghai 201800, China

ARTICLE INFO

*Keywords:*
Iodine
Adsorption
Sulfides
Heterogeneous interfaces
DFT calculations

ABSTRACT

We report a series of $MoS_2/CoS_2/Ni_3S_2$/NF heterogeneous interfaces with multiple types of adsorption sites, which exhibit excellent iodine capture performance. The optimized $MoS_2/CoS_2/Ni_3S_2$/NF-13 obtained at Mo:Co molar ratio of 1:3 shows an extremely large maximum iodine capture of 1804 mg/g. For the including component of $Ni_3S_2$/NF, REDOX reaction between $Ni^0/S^{2-}$ and $I_2$ offers the main driving force of chemisorption toward iodine (forming $NiI_2$ and $S_8$), while for $MoS_2$, the electrostatic adsorption makes the main contribution to the iodine capture, and for $CoS_2$, interfacial interactions promote the uptake capability of iodine. We perform density functional theory (DFT) calculations to determine the iodine adsorption energies ($E_{ad}$), which show that in $Ni_3S_2$ the Ni and S both serve as iodine sorption sites and Ni site binds more tightly to $I_2$ than S site does, while for $MoS_2$, the S site (rather than Mo) prefers to adsorb the $I_2$. X-ray absorption fine structures (XAFS) indicate that after iodine capture, oxidation states of Mo and Ni are increased more than that of Co, verifying $Ni_3S_2$ and $MoS_2$ interact more than $CoS_2$ on $I_2$. Though $CoS_2$ component does not directly adsorb $I_2$, interfacial electron transfers of Co → Ni and Co → Mo significantly promote iodine sorption capability. Synergistic effect of the multiple components/sites in the $MoS_2/CoS_2/Ni_3S_2$/NF assembly offers the wonderful iodine capture. This work provides a novel perspective and theoretical reference for tailoring effective metal sulfides-based sorbents to trap iodine from radioactive wastes.

## 1. Introduction

The worsening contradiction between rapid productivity growth and energy shortage compels us to accelerate the development of new sustainable energy sources to alleviate the current pressure on global energy supply and demand [1,2]. The nuclear energy is one of the best alternatives to traditional fossil energy due to its reliability and cost-effectiveness [3–5]. However, the management of radioactive waste from nuclear fission is a major challenge [6]. In particular, radioiodine isotopes ($^{129}I$ and $^{131}I$) pose serious threats to human health and ecological environment. Among them, $^{129}I$ possesses the characteristics of long half-life ($1.57 \times 10^7$ years), strong toxicity and high mobility, and easily leads to thyroid cancer after entering the human body [7,8]. Although the $^{131}I$ has a relatively short half-life (about 8 days), its intense radiation severely interferes with human metabolic process [9–11]. Therefore, the development of effective methods for capturing the radioactive iodine is of great significance.

Currently, the treatment of radioactive iodine mainly relies on wet washing and solid adsorption methods [12,13]. The solid adsorption is preferred because of its simple operation, low maintenance cost, and avoidance of using highly corrosive solutions [14–16]. Consequently, more and more researchers are committed to tailoring various sorbent materials, such as Ag-based materials [5,17–20], zeolites materials [6,21,22], carbon materials [23,24], sulfide materials [25,26],

* Corresponding authors.
*E-mail addresses:* yaohq@nxmu.edu.cn (H. Yao), hongliang.dong@hpstar.ac.cn (H. Dong), licheng@sinap.ac.cn (C. Li), mashulan@bnu.edu.cn (S. Ma).
[1] Present address: Experimental High School Attached to Beijing Normal University, Beijing 100032, China.

https://doi.org/10.1016/j.cej.2024.152514
Received 30 March 2024; Received in revised form 17 May 2024; Accepted 22 May 2024
Available online 23 May 2024


**Scheme 1.** Schematic illustration of $MoS_2/CoS_2/Ni_3S_2$/NF formation.

metal–organic frameworks (MOFs) [27,28], and covalent organic frameworks (COFs) [29,30]. Based on Hard and Soft Acids and Bases (HSAB) theory, the sulfides as soft Lewis bases show strong affinity with the soft Lewis acid of $I_2$ [31]. Subrahmanyam et al. [25] prepared $NiMoS_4$ and $CoMoS_4$ aerogels which captured iodine vapor via soft acid-soft base affinity, exhibiting the maximum iodine capture capacities ($q_m^I$) of 2250 and 2000 mg/g, respectively. Li et al. [32] reported that $Bi_2S_3$@$SiO_2$ achieved immobilization of iodine vapor via REDOX reaction between $S^{2-}$ and $I_2$, showing a $q_m^I$ of 1180 mg/g. Moreover, our group reported the $[Sn_2S_6]^{4-}$ and $[Mo_3S_{13}]^{2-}$ intercalated Mg/Al-type layered double hydroxides (MgAl-$Sn_2S_6$-LDH and MgAl-$Mo_3S_{13}$-LDH) which exhibited large $q_m^I$ values of 2954 and 1580 mg/g, respectively [33,34]. Importantly, the polysulfide clusters of $[Sn_2S_6]^{4-}$ and $[Mo_3S_{13}]^{2-}$ played major roles in the iodine capture. These studies demonstrated the unmatched potential of sulfide-based materials for iodine capture.

$I_2$ is a superior electron acceptor, and the charge transfer between iodine and sorbents may effectively improve the adsorption ability [2,29,35]. From density functional theory (DFT) calculations, Zhang et al. [36] demonstrated that $I_2$ was adsorbed on the surface of $MoS_2$ via electrostatic interaction, and charge transfer from Mo/S to $I_2$ occurred when $I_2$ molecules were vertically adsorbed to the surface of $MoS_2$. In addition, as reported by Komarov et al. [37], iodine could be chemically adsorbed on the (1 1 0) plane of Ni forming $NiI_2$. Moreover, our group reported *n*-$Ni_xS_y$/NF (NF is Ni foam) composites, among which the 1-$Ni_3S_2$/NF possessed the highest iodine adsorption capacity of 1445 mg/g) [38]. During the iodine adsorption, the $Ni^0/S^{2-}$ in $Ni_xS_y$ and $Ni^0$ in NF acted as reductants to reduce $I_2$, while they were oxidized to $Ni^{2+}$ (which combined with the resulting $I^-$ forming $NiI_2$) and $S_8$, respectively. Wu et. al [39] reported that Co-MOF with a ship-topology exhibited an adsorption capacity of 1080 mg/g for iodine vapor due to the conjugated π-electrons and REDOX potential of $Co^{2+}/Co^{3+}$. In addition, Lin et. al [40] demonstrated that tetrazole ring, coordination water and REDOX potential of $Co^{2+}/Co^{3+}$ in porous Co(II)-MOF all contributed to the iodine capture, giving a large $q_m^I$ of 2880 mg/g. Based on these studies, we propose a strategy for designing transition-metal sulfides assembly containing multiple sorption sites to achieve synergistic capture of iodine.

Herein, a series of $MoS_2/CoS_2/Ni_3S_2$/NF-*xy* composites (*x* and *y* refer to molar ratio of Mo:Co in the starting materials) are constructed by a facile one-step hydrothermal method. The $MoS_2/CoS_2/Ni_3S_2$/NF-13 (Mo:Co = 1:3) exhibits the best iodine capture performance, giving a $q_m^I$ of 1804 mg/g. The thin nanosheets coated on the nanorods of the $MoS_2/CoS_2/Ni_3S_2$/NF-13 provide abundant adsorption sites for trapping iodine. More importantly, based on the HSAB interactions, the high affinity of $MoS_2/CoS_2/Ni_3S_2$/NF with iodine leads to the capture of a large amount of $I_2$, most of which undergo REDOX reaction with $Ni_3S_2$, and partial $I_2$ molecules are electrostatically adsorbed on the interfaces of $MoS_2/Ni_3S_2$ and $MoS_2/CoS_2$. In addition, interfacial electron transfers of Co → Ni and Co → Mo further promote the iodine uptake. The iodine capture mechanism of the including metal sulfides is explored by DFT calculations, providing important theoretical basis for tailoring metal sulfide-based adsorbents to trap radioactive iodine.

## 2. Experimental section

### 2.1. Synthesis of $MoS_2/CoS_2/Ni_3S_2$/NF-xy

Based on previous work of $MoS_2/Co_9S_8/Ni_3S_2$/NF [41], through regulating the dosage of Mo, Co and S, hydrazine hydrate and NF, a series of $MoS_2/CoS_2/Ni_3S_2$/NF-*xy* (where *x* and *y* are molar ratios of Mo:Co) were obtained via one-step hydrothermal reaction (see Scheme 1). For $MoS_2/CoS_2/Ni_3S_2$/NF-13, firstly, 6 pieces of commercial NF (3 × 2 $cm^2$) were washed with HCl solution with a concentration of 1 M, acetone, deionized water and ethanol successively to remove the oxide layer and impurities on the NF surface. Meanwhile, 1 mmol of $Na_2MoO_4{\cdot}2H_2O$, 3 mmol of $CoSO_4{\cdot}7H_2O$ and 1 g of $CH_4N_2S$ were dissolved in 40 mL of deionized water, followed by 8 mL of hydrazine hydrate under stirring. Then the above solution and the pretreated NF were transferred into a 100 mL Teflon-lined steel autoclave, heated to 200 °C and kept for 24 h. After the reaction, the product was sequentially rinsed with deionized water and ethanol, and then dried overnight under vacuum at 45 °C, labeled as $MoS_2/CoS_2/Ni_3S_2$/NF-13.

Similar to the above experiments, the dosage of $Na_2MoO_4{\cdot}2H_2O$ was fixed at 1 mmol and that of Co was changed, with the Mo:Co molar ratios of 1:1 and 1:4, obtaining the $MoS_2/CoS_2/Ni_3S_2$/NF-11 and $MoS_2/CoS_2/Ni_3S_2$/NF-14, respectively.

The control samples of $MoS_2/Ni_3S_2$/NF and $CoS_2/Ni_3S_2$/NF were prepared in a similar procedure as $MoS_2/CoS_2/Ni_3S_2$/NF-*xy* except only adding Mo (1 mmol) or Co (1 mmol). Additionally, the $Ni_3S_2$/NF was prepared without Co/Mo addition and other conditions remained unchanged.

### 2.2. Iodine adsorption experiments

Since non-radioactive iodine has the same chemical properties as $^{129}I$ and $^{131}I$, we used non-radioactive iodine to generate iodine vapor in all adsorption experiments. The device shown in Fig. S1 was used for iodine capture experiments. Specifically, 1 g of $I_2$ solid was put into the bottom of a vial to provide iodine vapor after heating, and 5 mg of sorbent was placed in a conical filter paper above the iodine solid, with no direct contact between the sorbent and iodine solid. The sealed vial was placed into a larger bottle, which was tightly sealed and placed in an oven to heat to 80 °C and kept for 24 h. After the adsorption, the vial was quickly transferred to the fume hood and opened, and the residual iodine vapor escaped. After cooling to room temperature, the iodine capture capacity

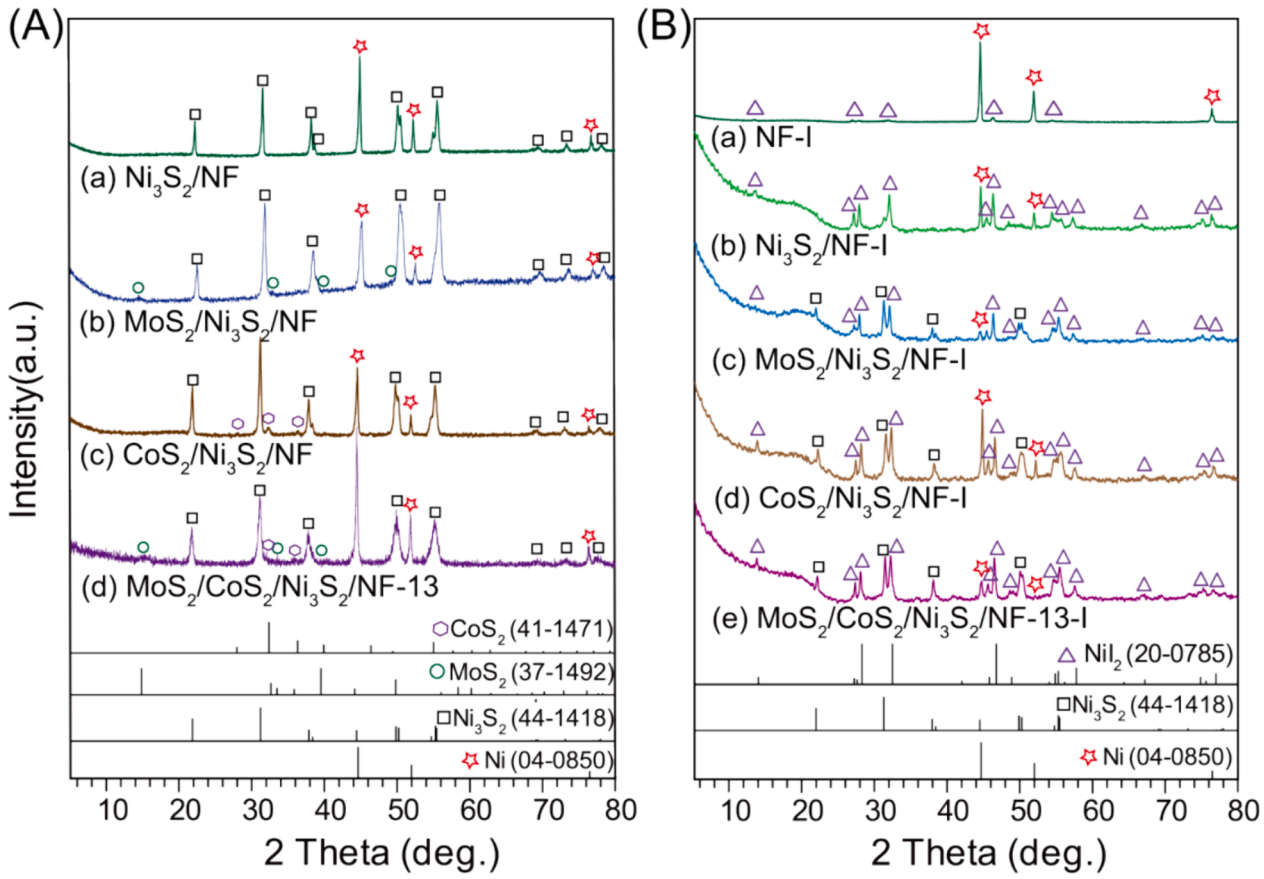


**Fig. 1.** (A) XRD patterns of (a) $Ni_3S_2$/NF, (b) $MoS_2/Ni_3S_2$/NF, (c) $CoS_2/Ni_3S_2$/NF and (d) $MoS_2/CoS_2/Ni_3S_2$/NF-13, and (B) XRD patterns after iodine capture: (a) NF-I, (b) $Ni_3S_2$/NF-I, (c) $MoS_2/Ni_3S_2$/NF-I, (d) $CoS_2/Ni_3S_2$/NF-I and (e) $MoS_2/CoS_2/Ni_3S_2$/NF-13-I.

of the sorbent was estimated based on the change in weight before and after iodine capture. For each static adsorption experiment, three groups were carried out in parallel. The iodine capture capacity was calculated according to Eq. (1), and the average value of the results was used for follow analysis.

$$q_e(\mathrm{mg/g}) = \frac{m_2 - m_1}{m_1} \times 1000 \quad (1)$$

where $q_e$ (mg/g) represents the amount of iodine adsorption, $m_1$ (mg) and $m_2$ (mg) represent the weights of the sorbent before and after iodine capture, respectively.

For sorption kinetics, the experimental procedures were similar to above, but changed the contact time to 30, 60, 90, 120, 150, 180, 240, 360, 540 and 720 min, and the amounts of iodine adsorbed were calculated by Eq. (1).

### 2.3. Desorption experiments

In order to figure out the release of adsorbed iodine, desorption experiments were performed by treating the post-sorption samples at 80 °C for 2 h under a vacuum degree of 0.09 MPa. The initial mass of the adsorbent was labeled as $m_1$ (the same as $m_1$ in formula 1), and the mass of the I-loaded sample after desorption was labeled as $m_2'$. According to the remaining mass, iodine adsorption capacity after desorption is calculated by Eq. (2).

$$q_e(\mathrm{mg/g}) = \frac{m_2' - m_1}{m_1} \times 1000 \quad (2)$$

where $q_e$ is iodine sorption capacity after desorption, $m_1$ (mg) is the initial mass of the sorbent, and $m_2'$ (mg) is the mass of the I-loaded sample after desorption.

### 2.4. XAFS measurements

X-ray absorption fine structure (XAFS) was collected in fluorescence mode using a Lytle detector under ambient conditions. The photon energies were calibrated using the first inflection point of the K-edges from metallic Mo, Ni and Co foils, respectively. All data were processed using ATHENA and ARTEMIS programs in the Demeter computer package.

### 2.5. DFT calculations

First-principles calculations was performed using DFT [42] within project augmented wave method (PAW) [43] implemented in the Vienna *Ab initio* Simulation Package (VASP) [44]. Exchange and correlation energy is performed by Perdue-Burke-Ernzerhof (PBE) [45] version of the generalized gradient approximation (GGA). The $3 \times 3 \times 1$ supercell of $Ni_3S_2$, $5 \times 5 \times 1$ supercell of $MoS_2$ and $3 \times 3 \times 1$ supercell of $CoS_2$ were constructed to assemble the heterostructures of $MoS_2/Ni_3S_2$, $MoS_2/CoS_2$ ($MoS_2$ as the adsorption surface) and $CoS_2/MoS_2$ ($CoS_2$ as the adsorption surface). Then, a single gas molecule of $I_2$ was adsorbed on the surface of heterostructure as the adsorption model. A vacuum slab of 15 Å was employed along the *c* axis to prevent the interaction between two neighbouring surfaces. A $3 \times 3 \times 3$ k-points Monkhorst Pack grid was used for the Brillouin zone sampling. The energy cut-off of plane wave basis sets was 450 eV. During structural optimization, the atoms in the system were relaxed until the force on each atom was below than 0.01 eV/Å. The stability of $I_2$ at the adsorption site was evaluated by calculating the adsorption energy using the following Eq. (3):

$$\Delta E_{ad} = E_{I2+M} - E_M - E_{I2} \quad (3)$$

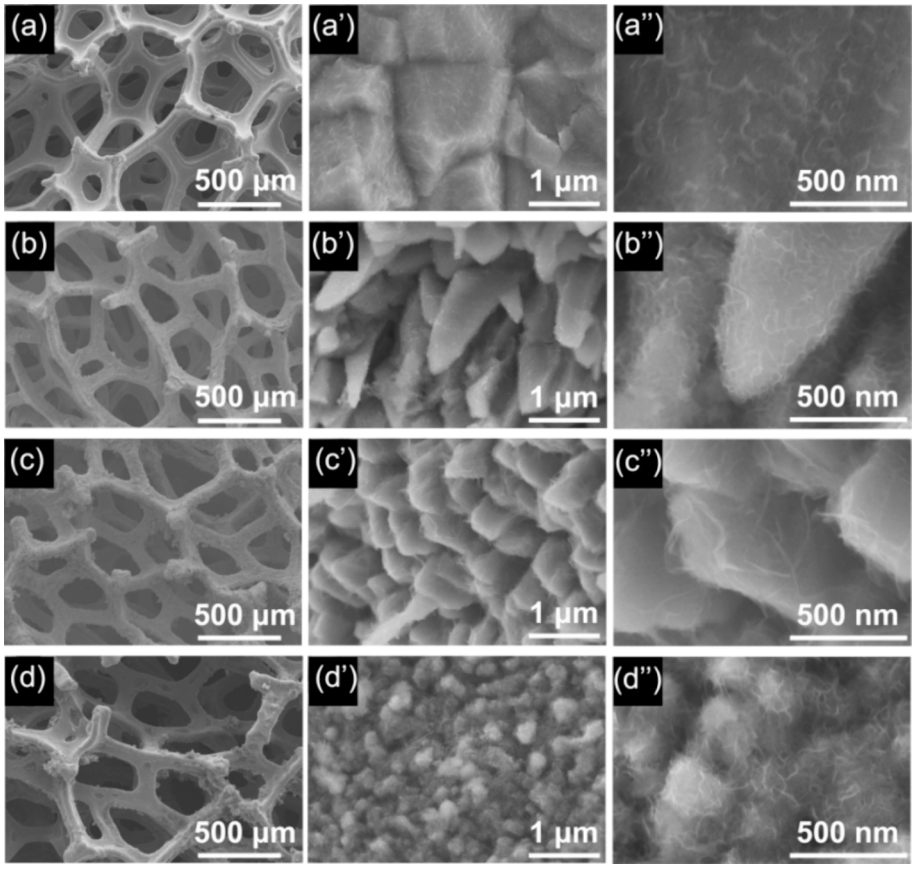


**Fig. 2.** SEM images of (a-a'') $Ni_3S_2$/NF, (b-b'') $MoS_2/Ni_3S_2$/NF, (c-c'') $CoS_2/Ni_3S_2$/NF and (d-d'') $MoS_2/CoS_2/Ni_3S_2$/NF-13.

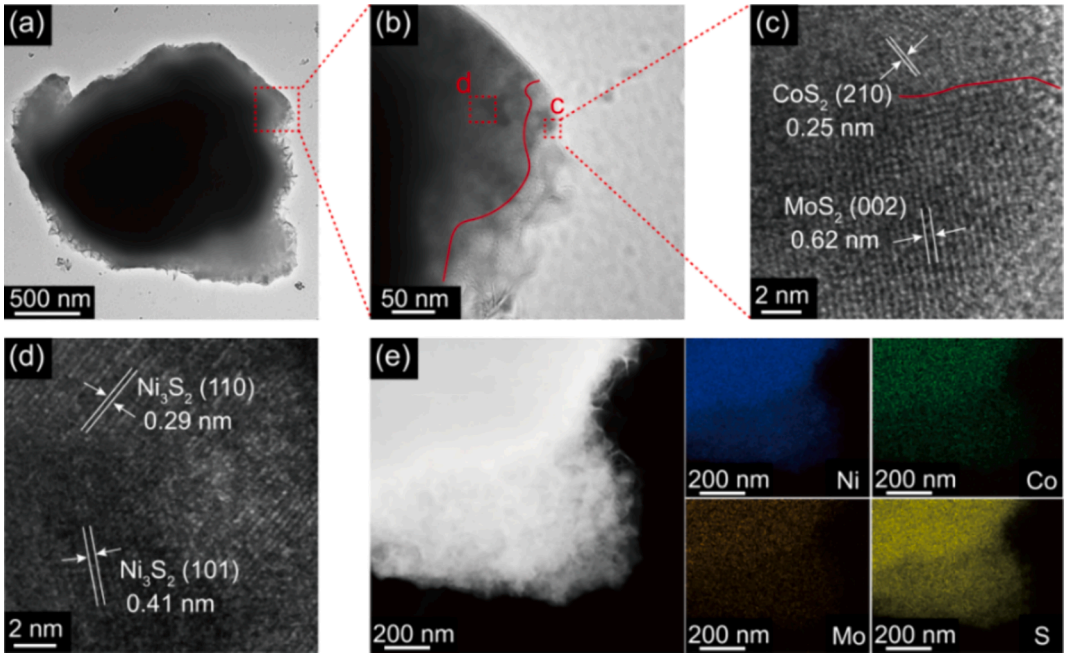


**Fig. 3.** (a, b) TEM images, (c, d) HRTEM images, (e) HAADF-STEM image and corresponding element mappings of Ni, Co, Mo, S in $MoS_2/CoS_2/Ni_3S_2$/NF-13.

where the $E_{I2+M}$ and $E_M$ are the total energy of the material with and without the $I_2$ molecule adsorbed on it, respectively, and the $E_{I2}$ is the total energy of a free $I_2$ molecule.

## 3. Results and discussion

### 3.1. Characterization of sorbents

The $MoS_2/CoS_2/Ni_3S_2$/NF-*xy* composites are fabricated via adjusting

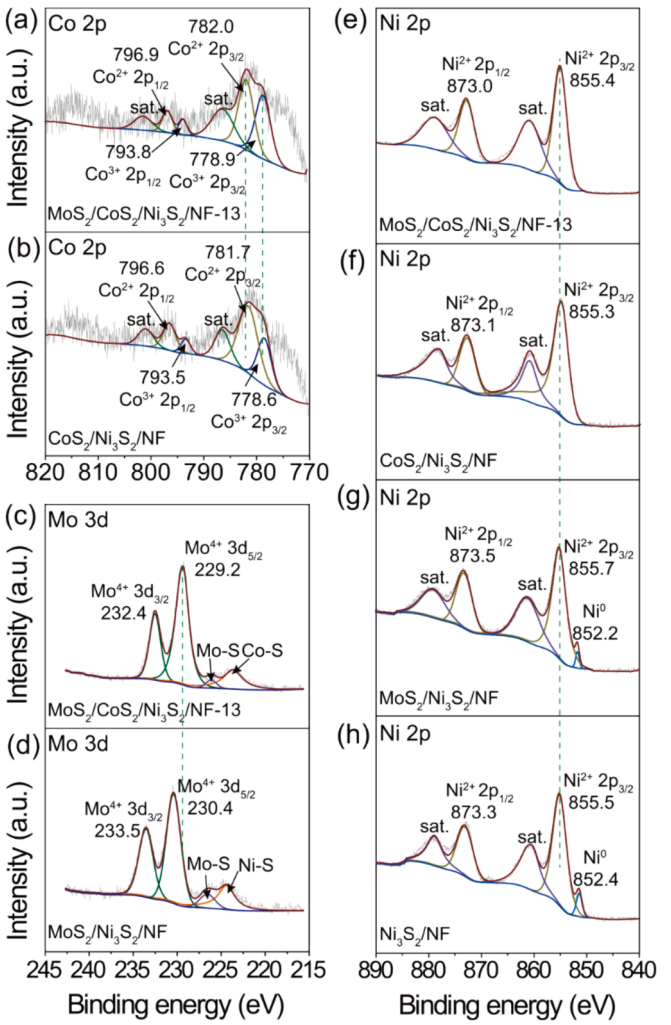


**Fig. 4.** XPS spectra of (a) Co 2p, (c) Mo 3d and (e) Ni 2p of $MoS_2/CoS_2/Ni_3S_2$/NF-13, (b) Co 2p and (f) Ni 2p of $CoS_2/Ni_3S_2$/NF, (d) Mo 3d and (g) Ni 2p of $MoS_2/Ni_3S_2$/NF, and (h) Ni 2p of $Ni_3S_2$/NF.

the dosage of Mo and Co salts with NF as Ni source (as shown in Scheme1). The following reactions may occur in the hydrothermal process [38,41]: First, the decomposition of $NH_2CSNH_2$ releases $HS^-$ ions (reaction (4)), which then react with Ni (NF) to form $Ni_3S_2$ (reaction (5)). Meanwhile, $MoO_4^{2-}$ and $Co^{2+}$ combine with $HS^-$ ions producing $MoS_2$ (reaction (6)) and $CoS_2$ (reaction (7)), respectively. During the hydrothermal process, NF acts as both the supporting skeleton for the growth of metal sulfides and the Ni source for the generation of $Ni_3S_2$ phase.

$$NH_2CSNH_2 + 3H_2O \rightarrow 2NH_4^+ + HS^- + HCO_3^- \quad (4)$$

$$3Ni + 2HS^- + 2H_2O \rightarrow Ni_3S_2 + 2OH^- + 2H_2 \quad (5)$$

$$2MoO_4^{2-} + 4HS^- + N_2H_4 \rightarrow 2MoS_2 + N_2 + 8OH^- \quad (6)$$

$$Co^{2+} + 2HS^- \rightarrow CoS_2 + H_2 \quad (7)$$

X-ray diffraction (XRD) was performed to study the crystal structures of the resulting products. For $Ni_3S_2$/NF (Fig. 1A–a), the peaks at $2\theta$ = 44.5°, 51.8° and 76.4° correspond to the (1 1 1), (2 0 0) and (2 2 0) planes of $Ni^0$ (JCPDS No. 04–0850) of NF, respectively. The XRD diffractions at 21.8°, 31.1°, 37.8°, 44.3°, 50.1° and 55.3° are ascribed to the (1 0 1), (1 1 0), (0 0 3), (2 0 2), (2 1 1) and (3 0 0) planes of $Ni_3S_2$ (JCPDS No. 44–1418). The presence of $Ni_3S_2$ and Ni in all products implies the partial sulfurization of the NF during the hydrothermal process. With the addition of only Mo salt (Fig. 1A–b), besides the $Ni_3S_2$ and $Ni^0$ phases, there appear diffraction peaks at $2\theta$ = 14.4°, 32.7°, 39.4° and 49.8° assigned to the (0 0 2), (1 0 0), (1 0 3) and (1 0 5) planes of $MoS_2$ (JCPDS No. 37–1492), confirming the generation of $MoS_2$. When only Co salt was added, as shown in Fig. 1A–c, the peaks observed at $2\theta$ = 27.9°, 32.4° and 36.1° are ascribed to the (1 1 1), (2 0 0) and (2 1 0) crystal planes of $CoS_2$ (JCPDS No. 41–1471), indicating the formation of $CoS_2$. Fig. 1A–d describes the XRD pattern of the as-prepared sample by the simultaneous addition of Mo and Co sources at Mo:Co molar ratio of 1:3. The presence of diffraction peaks of the three phases of $MoS_2$ and $CoS_2$ and $Ni_3S_2$ indicates the successful preparation of the $MoS_2/CoS_2/Ni_3S_2$/NF-13. In Fig. S2, the $MoS_2/CoS_2/Ni_3S_2$/NF-*xy* composites with different Mo:Co ratios have similar crystal structure, and the diffraction peaks of $CoS_2$ are slightly enhanced following the increase of Co content.

Scanning electron microscopy (SEM) was used to characterize the microscopic morphology of the samples. From Fig. 2a, b, c and d, it is observed that all samples well maintain the three-dimensional (3D) framework structure of NF (Fig. S3). For $Ni_3S_2$/NF (Fig. 2a'–a''), the magnified images reveal some small bumps with rough surface in striking contrast to the smooth surface of the pristine NF (Fig. S3). After introducing Mo salts, the nanorods arrays (~500 nm diameter for one rod, and the rods have a cone-shaped tip) are observed on the NF skeleton, and the nanorods are coated with many thin nanosheets (Fig. 2b'–b''). When only introducing Co salts, the obtained $CoS_2/Ni_3S_2$/NF exhibits similar morphology to that of $MoS_2/Ni_3S_2$/NF, but the nanorods of $CoS_2/Ni_3S_2$/NF are relatively shorter (the cone tip disappears) in length and larger in diameter (about 1 μm) (Fig. 2c'–c''). The composites of $MoS_2/CoS_2/Ni_3S_2$/NF-*xy* with both Mo and Co addition generally exhibit the morphology of nanorods coated with nanosheets, and the Co content affects the morphology significantly. For the $MoS_2/CoS_2/Ni_3S_2$/NF-13 at the Mo:Co ratio of 1:3 (Fig. 2d'–d''), the nanosheets are fluffier and the nanorods dimeter is smaller than that of the product with more Co content ($MoS_2/CoS_2/Ni_3S_2$/NF-14, see Fig. S4a–a''). At low Co dosage, the nanosheets on the surface of $MoS_2/CoS_2/Ni_3S_2$/NF-11 (Fig. S4b–b'') are fewer, and the exposed nanorods become smaller in diameter and longer in length.

Transmission electron microscope (TEM) was carried out to investigate the microstructure of the $MoS_2/CoS_2/Ni_3S_2$/NF-13. As depicted in Fig. 3a,b, thin nanosheets are tightly grown on the nanorod. The high-resolution TEM (HR-TEM) image (as shown in Fig. 3c) of the *c* region in Fig. 3b shows a clear interface between the (2 1 0) plane of $CoS_2$ (with 0.25 nm spacing) and the (0 0 2) plane of $MoS_2$ (with 0.62 nm spacing). The lattice fringes with spacings of 0.29 and 0.41 nm are observed in Fig. 3d (HR-TEM image of the *d* region in Fig. 3b), which are assigned to the (1 1 0) and (1 0 1) crystal planes of $Ni_3S_2$, respectively. These indicate that the nanorod belongs to the $Ni_3S_2$ phase, whose surface is covered with the nanosheets of $CoS_2$ and $MoS_2$. The corresponding elemental maps (Fig. 3e) from the high-angle ring dark field scanning transmission electron microscopy (HAADF-STEM) show that the elements of Ni, Co, Mo, and S are distributed in the $MoS_2/CoS_2/Ni_3S_2$/NF-13.

Elemental chemical states of the materials were analyzed by X-ray photoelectron spectroscopy (XPS). For $MoS_2/CoS_2/Ni_3S_2$/NF-13, the Co 2p spectrum (Fig. 4a) is divided into two spin orbit twin peaks and two satellite peaks (marked by "Sat."), where the peaks at 778.9 and 793.8 eV are allocated to $2p_{3/2}$ and $2p_{1/2}$ of $Co^{3+}$ [46,47], and the signals observed at 782.0 and 796.9 eV are assigned to $2p_{3/2}$ and $2p_{1/2}$ of $Co^{2+}$, respectively [48]. For Mo 3d (Fig. 4c), the 229.2 and 232.4 eV belong to $3d_{5/2}$ and $3d_{3/2}$ of $Mo^{4+}$ [49,50]. In Ni 2p (as described in Fig. 4e), the peaks at 855.4 and 873.0 eV are attributed to $2p_{3/2}$ and $2p_{1/2}$ of $Ni^{2+}$, respectively [51,52]. For S 2p (Fig. S5a), the two peaks at 164.2 and 162.9 eV correspond to S $2p_{1/2}$ and S $2p_{3/2}$ of $S_2^{2-}$ arising from the S-S bridges in $CoS_2$ and terminal unsaturated S of $MoS_2$ [48,53], and the peaks at 163.3 and 162.0 eV belong to S $2p_{1/2}$ and S $2p_{3/2}$ of $S^{2-}$ [54,55]. Moreover, the binding energy of 168.4 eV (Fig. S5a) is related to the S-O bonding produced by surface oxidation of the material [56].

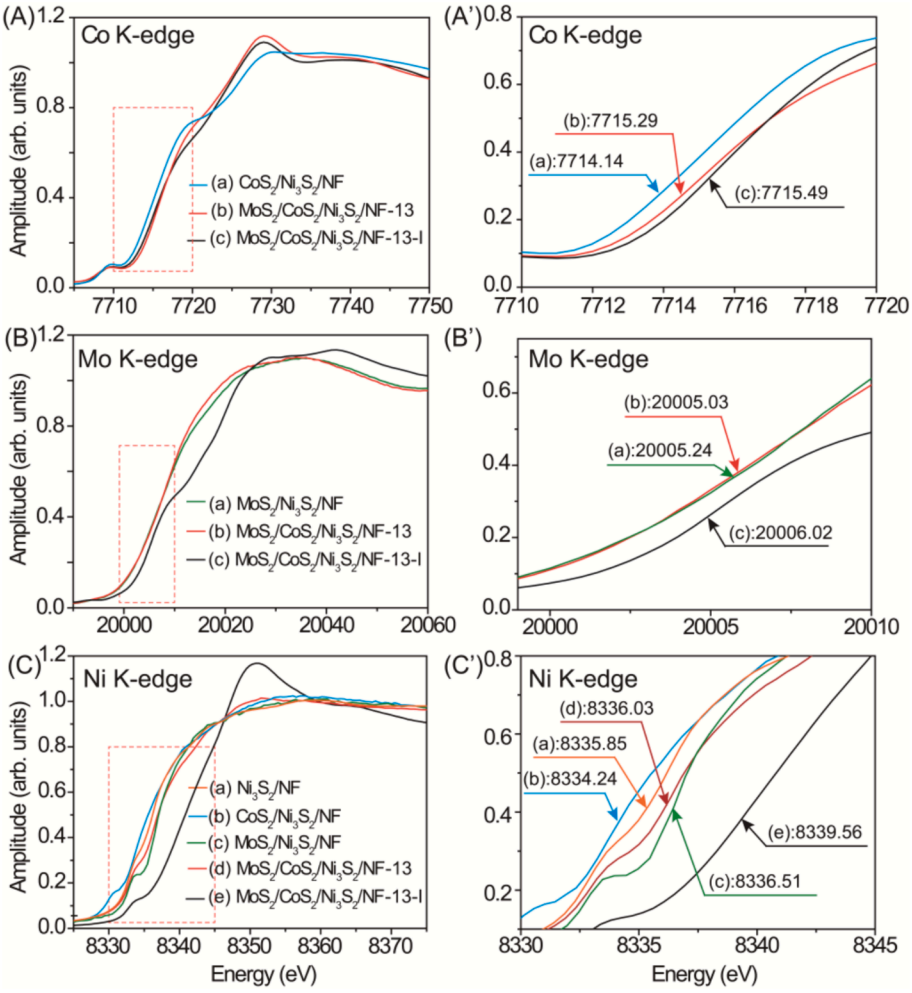


**Fig. 5.** (A) Co K-edge XANES and (A') an enlarged image corresponding to the red areas of (a) $CoS_2/Ni_3S_2$/NF, (b) $MoS_2/CoS_2/Ni_3S_2$/NF-13 and (c) $MoS_2/CoS_2/Ni_3S_2$/NF-13-I, (B) Mo K-edge XANES and (B') an enlarged images corresponding to the red areas of (a) $MoS_2/Ni_3S_2$/NF, (b) $MoS_2/CoS_2/Ni_3S_2$/NF-13 and (c) $MoS_2/CoS_2/Ni_3S_2$/NF-13-I, (C) Ni K-edge XANES and (C') an enlarged images corresponding to the red areas of (a) $Ni_3S_2$/NF, (b) $CoS_2/Ni_3S_2$/NF, (c) $MoS_2/Ni_3S_2$/NF, (d) $MoS_2/CoS_2/Ni_3S_2$/NF-13 and (e) $MoS_2/CoS_2/Ni_3S_2$/NF-13-I. (For interpretation of the references to colour in this figure legend, the reader is referred to the web version of this article.)

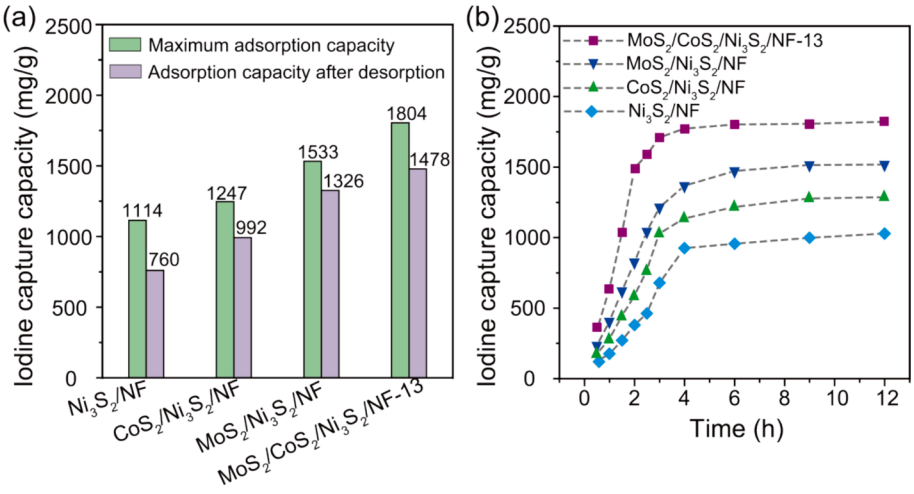


**Fig. 6.** (a) Iodine capture capacities and (b) sorption kinetics of $Ni_3S_2$/NF, $CoS_2/Ni_3S_2$/NF, $MoS_2/Ni_3S_2$/NF and $MoS_2/CoS_2/Ni_3S_2$/NF-13.

**Table 1**
Adsorption capacity of $I_2$ by $MoS_2/CoS_2/Ni_3S_2$/NF-13 and reported materials.

| Sorbents | T (°C) | Iodine capture capacity (mg/g) | References |
|---|---|---|---|
| **$MoS_2/CoS_2/Ni_3S_2$/NF** | **80** | **1804** | **This work** |
| $Ni_xS_y$/NF[a] | 77 | 1442 | *Chem. Eng. J. 2024.* [38] |
| $Bi_2S_3$@$SiO_2$[b] | 200 | 1180 | *ACS Appl. Nano Mater. 2023.* [32] |
| NaY-$NH_4F$-$Bi_2S_3$[c] | 75 | 491 | *Chem. Eng. J. 2022.* [57] |
| MgAl-$Mo_3S_{13}$-LDH[d] | 80 | 1580 | *J. Colloid Interface Sci. 2024.* [34] |
| NiTi-$S_x$-LDH[e] | 75 | 520 | *Chem. Eng. J. 2019.* [60] |
| BiZnAl-LDH[f] | 75 | 433 | *RSC Adv. 2020.* [58] |
| $NiMoS_4$[g] | 200 | 2250 | *Chem. Mater. 2015.* [25] |
| $CoMoS_4$[h] | 75 | 2000 | *Chem. Mater. 2015.* [25] |
| KCoS[i] | 75 | 1600 | *Chem. Mater. 2015.* [25] |
| $MoS_{x\ aerogel}$[j] | 60 | 1000 | *J. Am. Chem. Soc. 2015.* [26] |
| $Ag^0$@BT-nCF[k] | 75 | 1704 | *Appl. Surf. Sci. 2022.* [17] |
| AgX[l] | 150 | 355 | *Ind. Eng. Chem. Res. 2023.* [61] |
| Ag/Cu-BTC-DMA[m] | 80 | 410 | *ACS Appl. Nano Mater. 2023.* [62] |
| Cu-BTC@PES[n] | 75 | 639 | *Appl. Mater. Interfaces 2019.* [59] |

[a] $Ni_xS_y$/NF, fabricated by one-step hydrothermal reaction with nickel foam and thiourea as raw materials.
[b] $Bi_2S_3$@$SiO_2$, prepared via coating $Bi_2S_3$ with electrospinning $SiO_2$ nanofiber.
[c] NaY-$NH_4F$-$Bi_2S_3$, fabricated by modifying bismuth sulfide supported NaY zeolite with fluoride.
[d] MgAl-$Mo_3S_{13}$-LDH, obtained by introducing $[Mo_3S_{13}]^{2-}$ into MgAl-LDH interlayers.
[e] NiTi-$S_x$-LDH with NiTi-LDH layers and polysulfides.
[f] BiZnAl-LDH obtained via bismuth modified ZnAl-LDH.
[g] NiMoS4, fabricated via mixing $(NH_4)_2MoS_4$ with $NiCl_2$ in formamide followed supercritical drying.
[h] $CoMoS_4$, obtained by mixing $(NH_4)_2MoS_4$ with $CoCl_2$ in formamide followed supercritical drying.
[i] KCoS, fabricated by mixing $K_2S_5$ with $CoCl_2$ in formamide followed supercritical drying.
[j] $MoS_{x\ aerogel}$, synthesized by an oxidative coupling using $(NH_4)_2MoS_4$ and iodine.
[k] $Ag^0$@BT-nCF, synthesized through chemical cross-linking and redox methods with collagen fiber as raw materials.
[l] AgX, Ag-based zeolite material.
[m] Ag/Cu-BTC-DMA, fabricated by cation exchange with $[(CH_3)_2NH_2]_3[(Cu_4Cl)_3(BTC)_8]\cdot 9DMA$ (Cu-BTC-DMA) as precursor.
[n] Cu-BTC@PES, millimeter-scale porous Cu-BTC@poly(ether sulfone) composite prepared by a phase inversion method.

To explore effects of Mo and Co on the electronic structure of the $MoS_2/CoS_2/Ni_3S_2$/NF, XPS tests of control samples of $Ni_3S_2$/NF, $CoS_2/Ni_3S_2$/NF and $MoS_2/Ni_3S_2$/NF were also performed. Compared with Co 2p (Fig. 4b) and Ni 2p (Fig. 4f) spectra of $CoS_2/Ni_3S_2$/NF, the peak positions of $MoS_2/CoS_2/Ni_3S_2$/NF-13 (Fig. 4a, e) shift to the direction of high binding energy (Co 2p shift is +0.3 eV, Ni 2p shift is +0.1 eV), demonstrating increased oxidation state of Co and Ni in the presence of Mo. Furthermore, a negative shift (-1.2 eV) is observed in the Mo 3d spectrum of $MoS_2/CoS_2/Ni_3S_2$/NF-13 (Fig. 4c) compared to $MoS_2/Ni_3S_2$/NF (without $CoS_2$) (Fig. 4d), which further proves the electron transfer from Co to Mo in $MoS_2/CoS_2/Ni_3S_2$/NF-13. Similarly, compared with $Ni_3S_2$/NF (Fig. 4h), the Ni 2p spectrum of $MoS_2/Ni_3S_2$/NF (Fig. 4g) shows a positive shift of +0.2 eV (from 855.5 to 855.7 eV), confirming the electron transfer of Ni → Mo. In addition, compared with $Ni_3S_2$/NF (Fig. 4h), the Ni 2p peak of $CoS_2/Ni_3S_2$/NF (Fig. 4f) in $CoS_2/Ni_3S_2$/NF exhibits a negative shift (from 855.5 to 855.3 eV), indicating that the presence of Co surely reduces the oxidation state of Ni. Moreover, no significant change is observed in S 2p peaks of $MoS_2/CoS_2/Ni_3S_2$/NF-13 and control samples (Fig. S5). These electron transfers in the $MoS_2/CoS_2/Ni_3S_2$/NF are also confirmed by the XAFS results below.

Fig. 5 depicts the XAFS of $MoS_2/CoS_2/Ni_3S_2$/NF-13 and control samples. The K-edges of Co, Mo and Ni are shown in Fig. 5A, B, C, for which the Fig. 5A', B', C' are the enlarged images corresponding to red areas on the left. Compared to $CoS_2/Ni_3S_2$/NF (Fig. 5A'–a), the absorption edges of Co in $MoS_2/CoS_2/Ni_3S_2$/NF-13 (Fig. 5A'–b) shifts to the higher energy (7714.14 → 7715.29 eV), and the absorption edges of Mo in $MoS_2/CoS_2/Ni_3S_2$/NF-13 (Fig. 5B'–b) shifts toward the lower energy (20005.24 → 20005.03 eV) compared to $MoS_2/Ni_3S_2$/NF (Fig. 5B'–a), proving the Co → Mo electron transfer. For the Ni K-edge, compared with $CoS_2/Ni_3S_2$/NF (no $MoS_2$, 8334.24 eV, see Fig. 5C'–b), the absorption edge of $MoS_2/CoS_2/Ni_3S_2$/NF-13 (with $MoS_2$, 8336.03 eV, see Fig. 5C'–d) shifts toward higher energy, and similar positive shift is observed in $MoS_2/Ni_3S_2$/NF (with $MoS_2$, 8336.51 eV, see Fig. 5C'–c) relative to $Ni_3S_2$/NF (without $MoS_2$, 8335.85 eV, see Fig. 5C'–a), both of which suggest electron transfer of Ni → Mo. Moreover, compared to $CoS_2$absent phases of $MoS_2/Ni_3S_2$/NF (8336.51 eV, Fig. 5C'–c) and $Ni_3S_2$/NF (8335.85 eV, Fig. 5C'–a), the Ni K-edge of $CoS_2$-containing phases of $MoS_2/CoS_2/Ni_3S_2$/NF-13 (8336.03 eV, Fig. 5C'–d) and $CoS_2/Ni_3S_2$/NF (8334.24 eV, see Fig. 5C'–b) shift to lower energy, respectively, demonstrating the electron transfer from Co to Ni. All the electron transfers of Ni → Mo, Co → Mo and Co → Ni would optimize the electronic structure, which is conducive to improving iodine adsorption performance discussed below.

### 3.2. Capture of iodine vapor

The maximum iodine capture capacity was assessed via the mass difference of sorbent before and after trapping iodine according to the formula (1). As described in Fig. S6, pure NF shows a much low iodine adsorption capacity of 160 mg/g. However, the iodine adsorption capacity of $MoS_2/CoS_2/Ni_3S_2$/NF-13 is significantly increased to 1804 mg/g, which is much larger than those of $MoS_2/CoS_2/Ni_3S_2$/NF-14 (1705 mg/g) and $MoS_2/CoS_2/Ni_3S_2$/NF-11 (1156 mg/g). The best iodine capture performance of $MoS_2/CoS_2/Ni_3S_2$/NF-13 may profit from the morphology of nanorods wrapped in fluffy thin nanosheets which provide more adsorption sites. Moreover, the iodine capture capacity of $MoS_2/CoS_2/Ni_3S_2$/NF-13 is also higher than those of $Ni_3S_2$/NF (1114 mg/g), $CoS_2/Ni_3S_2$/NF (1247 mg/g) and $MoS_2/Ni_3S_2$/NF (1533 mg/g) (shown in Fig. 6a). The significantly enhanced iodine capture ability of $MoS_2/CoS_2/Ni_3S_2$/NF-13 highlights the important role of interfacial interactions of the $CoS_2$, $MoS_2$ and $Ni_3S_2$. Notably, as listed in Table 1, the iodine capture capability of $MoS_2/CoS_2/Ni_3S_2$/NF-13 surpasses most of the existing inorganic sorbents [17,25,26,32,34,38,57–62], for example, metal sulfides ($Bi_2S_3$@$SiO_2$, $q_m^I$ = 1180 mg/g [32]; 1-$Ni_3S_2$/NF, $q_m^I$ = 1442 mg/g [35]; NaY-$NH_4F$-$Bi_2S_3$, $q_m^I$ = 491 mg/g [57]), and LDH-based sorbents ($Mo_3S_{13}$-LDH, $q_m^I$ = 1580 mg/g [31]; BiZnAl-LDH, $q_m^I$ = 433 mg/g [58]; NiTi-$S_x$-LDH, $q_m^I$ = 520 mg/g [60]), and is comparable to sulfur-based aerogels such as $NiMoS_4$ ($q_m^I$ = 2250 mg/g) and $CoMoS_4$ ($q_m^I$ = 2000 mg/g) [25].

To further investigate the contribution of physical adsorption and chemical adsorption on the iodine capture, the I-loaded samples were placed in a vacuum oven (vacuum degree is 0.09 MPa) at 80 °C for 2 h to perform the desorption experiments. As shown in Fig. 6a and Fig. S6, after being heated in the vacuum condition, the iodine adsorption capacities of all the samples show slight decrease. The capacity differences before and after desorption range in 207–354 mg/g, which are higher than the maximum iodine adsorption capacity of pristine NF (160 mg/g). This indicates that the released iodine under such desorption condition (80 °C heating and 0.09 MPa vacuum degree) is not only derived from physical adsorption, but also from chemisorption driven by soft acid-soft base interaction (labeled as HSAB-I). Furthermore, specific surface areas and pore characteristics of $MoS_2/CoS_2/Ni_3S_2$/NF-13 and control samples were studied via $N_2$ sorption measurements. As shown in Fig. S7, all samples show type-IV $N_2$ adsorption/desorption isotherms with $H_3$-type hysteresis loops, meaning mesoporous structures [33]. More importantly, although the specific surface area ($S_{BET}$ = 7.134 $m^2$

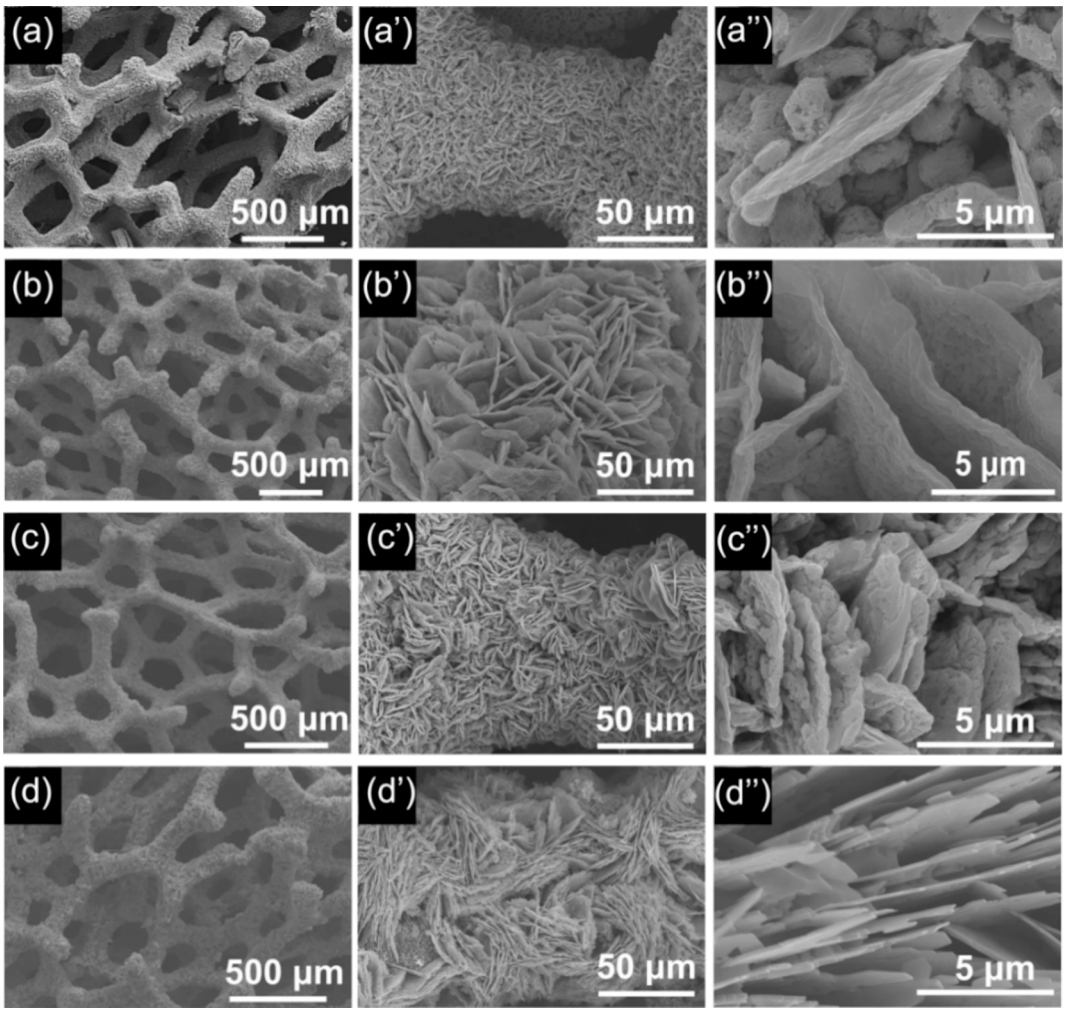


**Fig. 7.** SEM images of (a-a'') $Ni_3S_2$/NF-I, (b-b'') $MoS_2/Ni_3S_2$/NF-I, (c-c'') $CoS_2/Ni_3S_2$/NF-I and (d-d'') $MoS_2/CoS_2/Ni_3S_2$/NF-13-I.

$g^{-1}$), pore size (4.004 nm) and pore volume (0.021 cc/g) of $MoS_2/CoS_2/Ni_3S_2$/NF-13 are slightly larger than those of $Ni_3S_2$/NF ($S_{BET} = 0.596$ $m^2$ $g^{-1}$, 3.978 nm, 0.002 cc/g), $MoS_2/Ni_3S_2$/NF ($S_{BET} = 0.863$ $m^2$ $g^{-1}$, 3.989 nm, 0.003 cc/g) and $CoS_2/Ni_3S_2$/NF ($S_{BET} = 1.507$ $m^2$ $g^{-1}$, 4.000 nm, 0.004 cc/g), all the values are still small, indicating that the NF-based samples have small specific surface area and low porosity. This means weak physical adsorption ability toward iodine. After desorption, the $MoS_2/CoS_2/Ni_3S_2$/NF-13 still exhibits a very large iodine capacity of 1478 mg/g, which is attributed to the chemical adsorptions from the three phases of $MoS_2$, $CoS_2$ and $Ni_3S_2$.

The change of iodine sorption capacity with time was measured to investigate the sorption kinetics of $MoS_2/CoS_2/Ni_3S_2$/NF-13 and the control samples. As shown in Fig. 6b, the iodine absorption capacity of $MoS_2/CoS_2/Ni_3S_2$/NF-13 increases rapidly and reaches 80% of the equilibrium adsorption capacity within 2 h of the initial adsorption. With the extension of adsorption time, the adsorption rate gradually and slowly increases until adsorption equilibrium is reached, giving the maximum adsorption capacity (~1810 mg/g). In contrast, control samples of $Ni_3S_2$/NF (4 h), $CoS_2/Ni_3S_2$/NF (3 h) and $MoS_2/Ni_3S_2$/NF (3 h) require longer time to reach 80% of the equilibrium adsorption capacity. Interfacial interactions among $CoS_2$, $MoS_2$ and $Ni_3S_2$ in $MoS_2/CoS_2/Ni_3S_2$/NF-13 may be the main reason to accelerate the sorption kinetics.

### 3.3. Characterization of post-sorption samples and iodine capture mechanism

To investigate the sorption mechanism, XRD, SEM-EDS and XPS were utilized to characterize the I-loaded samples. As shown in Fig. 1B–a, after NF traps the iodine, the weak diffractions appear at $2\theta = 13.4°$, 26.6°, 27.7°, 31.9° and 48.3° correspond to the crystal planes of (0 0 3), (1 0 1), (0 1 2), (1 0 4) and (1 1 3) of $NiI_2$ (JCPDS No. 20–0785) besides the diffraction peaks of $Ni^0$. This indicates that the $Ni^0$ of NF skeleton can reduce $I_2$ molecules to $I^-$ ions, while the Ni itself is oxidized to $Ni^{2+}$, which combines with $I^-$ forming $NiI_2$. It is worth nothing that for $Ni_3S_2$/NF-I (Fig. 1B–b), the intensity of diffraction peaks related to $Ni^0$ decreases, and the peaks of $Ni_3S_2$ disappear, while the diffractions of $NiI_2$ are generated, implying that $Ni^0$ in $Ni_3S_2$ and NF acts as a reducing agent to realize chemisorption for iodine. Our recent work also confirmed the $Ni_3S_2$/NF could chemically adsorb the iodine, and $Ni_3S_2$ fully participated the sorption reaction with $I_2$ while NF partially took part in, so the NF skeleton could be well maintained [38]. For the materials containing other phases such as $MoS_2$ and/or $CoS_2$ besides the $Ni_3S_2$/NF, after iodine adsorption, as found in $MoS_2/Ni_3S_2$/NF-I (Fig. 1B–c), $CoS_2/Ni_3S_2$/NF-I (Fig. 1B–d) and $MoS_2/CoS_2/Ni_3S_2$/NF-13-I (Fig. 1B–e), besides the resulting $NiI_2$, the starting phase of $Ni_3S_2$ still exists, meaning incomplete reaction with $I_2$. This may be due to the coating of $MoS_2$ and/or $CoS_2$ nanosheets on the surface of $Ni_3S_2$ hinder its reaction in the inner layer with $I_2$. Furthermore, during the capture, no Mo/Co iodides are observed, which is consistent with previous reports [25,34]. Based on reference [63,64], $I^-$ thermodynamically favored the binding to

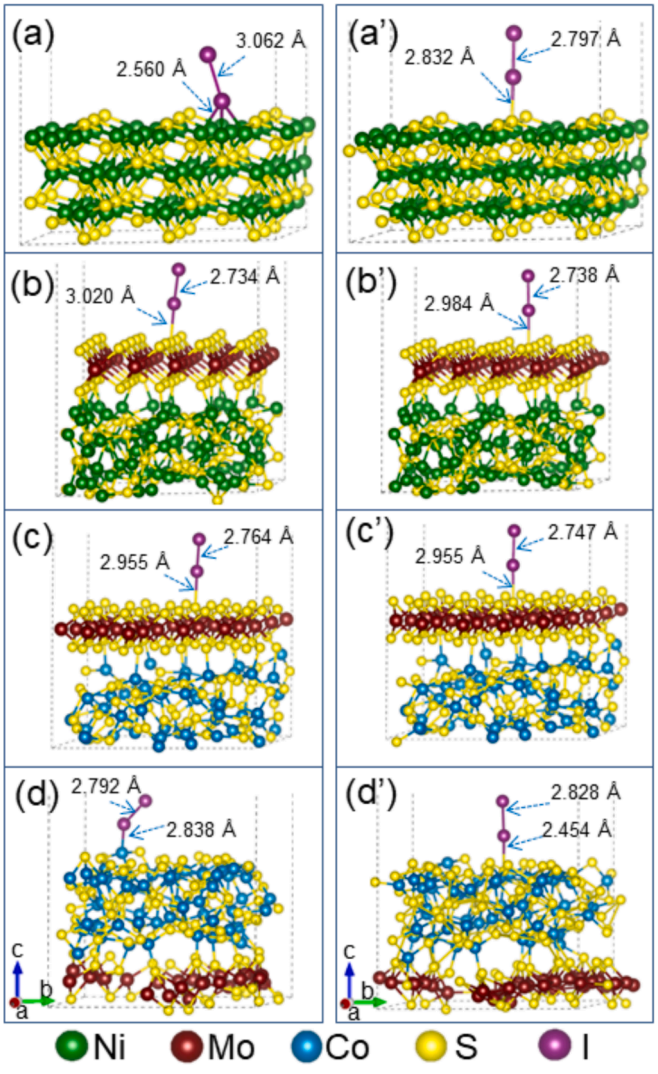


**Fig. 8.** Optimized structural models with one $I_2$ molecule adsorbed on the metal sites of (a) $Ni_3S_2$, (b) $MoS_2/Ni_3S_2$, (c) $MoS_2/CoS_2$ and (d) $CoS_2/MoS_2$, and S sites of (a') $Ni_3S_2$, (b') $MoS_2/Ni_3S_2$, (c') $MoS_2/CoS_2$ and (d') $CoS_2/MoS_2$.

$Mo^{2+}/Mo^{3+}$ rather than to $Mo^{4+}$, so $MoI_x$ compounds are not formed due to the +4 valence of Mo in $MoS_2$. In addition, the weak affinity of cobalt ions with $I^-$ [65] results in the absence of Co iodides. However, though not producing Mo/Co-based iodides, subsequent DFT calculations testify that the two phases of $MoS_2$ and $CoS_2$ still play important role during the adsorption.

Raman spectroscopy was measured to investigate the structure change of $MoS_2/CoS_2/Ni_3S_2$/NF-13 after iodine capture. As described in Fig. S8, the Raman shifts at 152 and 213 $cm^{-1}$ originate from the anti-symmetric stretching vibration and the bending vibration of $S_8$ ring, respectively [66,67]. Furthermore, the peak at 533 $cm^{-1}$ is associated with the $\nu(S\text{-}S)_{bri}$ [68]. These results demonstrate the formation of $S_8$, and also imply that $S^{2-}$ in $MoS_2/CoS_2/Ni_3S_2$/NF-13 is oxidized to $S_8$. The Raman shifts at the 388–285 $cm^{-1}$ correspond to the $\nu$(Mo-S) [69], suggesting the $MoS_2$ phase still exists in the post-sorption sample of $MoS_2/CoS_2/Ni_3S_2$/NF-13-I. Moreover, the signal at 118 $cm^{-1}$ is associated with Ni-I bond [70], implying the generation of $NiI_2$.

The morphologies of the samples after iodine sorption were characterized by SEM. From Fig. 7a,b,c,d, after iodine adsorption, the $MoS_2/CoS_2/Ni_3S_2$/NF-13-I and the control samples still well maintain the NF skeleton. For $Ni_3S_2$/NF-I (Fig. 7a',a''), many nanosheets crisscrossed on the NF skeleton are observed at high magnification, probably originating from the growth of $NiI_2$. For $MoS_2/Ni_3S_2$/NF-I (Fig. 7b',b''), there are more nanosheets growing tightly on the NF. The $CoS_2/Ni_3S_2$/NF-I has a similar morphology to $MoS_2/Ni_3S_2$/NF-I, expect the rougher surfaces of the nanosheets (Fig. 7c',c''). Notably, as described in Fig. 7d', d'', the morphology of $MoS_2/CoS_2/Ni_3S_2$/NF-13-I changes significantly compared with the control samples, with the nanosheets becoming longer in length while thinner in thickness. The elemental mapping of $MoS_2/CoS_2/Ni_3S_2$/NF-13-I shows that only Ni and I elements are found to be evenly distributed throughout the nanosheets (Fig. S9a1-a2), confirming that the nanosheets correspond to the $NiI_2$ phase. The Mo, Co and S elements have not been detected on the nanosheets, so we changed the detection area and performed the energy dispersive X-ray spectroscopy (EDS) again with the high magnification. We selected the region close to the NF substrate for EDS analysis. In Fig. S9b, the red region is the NF substrate, whose surface is covered with the abundant irregular substances. Outside the red area are $NiI_2$ nanosheets. From corresponding elemental mapping, it is observed that Ni element is distributed throughout the region (Fig. S9b–1), while the I element is concentrated on the $NiI_2$ nanosheets (Fig. S9b–5). Particular attention should be paid to the fact that Co, Mo and S elements (Fig. S9b–2, b–3 and b–4) are concentrated in the red region of Fig, S9b, implying that the substances may be $CoS_2$ and $MoS_2$ that have not reacted with $I_2$.

I-loaded samples were also characterized by XPS to study the elemental chemical states. The obvious I 3d signal in survey spectrum proves that the iodine molecules are trapped by $MoS_2/CoS_2/Ni_3S_2$/NF-13 (Fig. S10a). In the I 3d (Fig. S10b), the peaks at 618.9 and 630.3 eV are attributed to I $3d_{5/2}$ and I $3d_{3/2}$ of $I_3^-$ [71,72]. Compared with $MoS_2/CoS_2/Ni_3S_2$/NF-13 (Fig. 4e), the Ni 2p (Fig. S10c) of $MoS_2/CoS_2/Ni_3S_2$/NF-13-I is shifted +0.1 eV toward the higher binding energy, possibly due to the formation of $NiI_2$ with stronger electronegative $I^-$ (compared with $S^{2-}$ in $Ni_3S_2$). For Co 2p (see Fig. S10d), the peak positions exhibit positive shifts (+0.3 eV) and the ratio of fitted peak area of $Co^{3+}/Co^{2+}$ increases after iodine capture. As shown in Fig. S10e, compared with $MoS_2/CoS_2/Ni_3S_2$/NF-13 (Fig. 4c), the Mo 3d peak of Mo(IV) in $MoS_2/CoS_2/Ni_3S_2$/NF-13-I has a left-shift of +0.1 eV. In addition, the signals at 236.2 and 233.1 eV belong to Mo $3d_{3/2}$ and Mo $3d_{5/2}$ of $Mo^{6+}$ [73], and the a small amount of $Mo^{6+}$ may result from the surface oxidation of the sample. For S 2p spectrum (Fig. S10f), after iodine capture, the peak intensity associated with $S_2^{2-}/S^{2-}$ in $MoS_2/CoS_2/Ni_3S_2$/NF-13-I is significantly reduced, and the peak positions are shifted +0.2 eV towards higher energy. Moreover, a signal belonging to $S^0$ appears at 165.1 eV [60]. These results imply that $S_2^{2-}/S^{2-}$ species of $Ni_3S_2$ in $MoS_2/CoS_2/Ni_3S_2$/NF-13 are oxidized to $S_8$ during iodine adsorption.

Furthermore, the XAFS of the I-loaded sample of $MoS_2/CoS_2/Ni_3S_2$/NF-13-I was adopted to explore the change of chemical state of Co, Mo and Ni. As shown in Fig. 5A', B' and C', the absorption edges of Co (7715.29 → 7715.49 eV), Mo (20005.03 → 20006.02) and Ni (8336.03 → 8339.56 eV) show shifts of +0.20, +0.99 and +3.53 eV to higher energy, respectively after iodine capture, providing the increased oxidation states of the three metal ions after loading iodine. Importantly, compared with Co, the much increased oxidation states of Ni and Mo mean the $Ni_3S_2$ and $MoS_2$ have stronger interactions with iodine. The enormous variation in the absorption edges of Ni implies great change in the chemical environment, such as the phase transformation of $Ni_3S_2$ to $NiI_2$.

### 3.4. DFT calculations

In order to know about the interfacial effect of $MoS_2/CoS_2/Ni_3S_2$/NF on the iodine capture, as shown in Fig. S11, we constructed four structural models of $Ni_3S_2$, $MoS_2/Ni_3S_2$ ($MoS_2$ as adsorption surface), $MoS_2/CoS_2$ ($MoS_2$ as adsorption surface) and $CoS_2/MoS_2$ ($CoS_2$ as adsorption surface), and calculated the adsorption energy ($E_{ad}$) for $I_2$ using DFT. Firstly, a single $I_2$ molecule was optimized by DFT calculations. The calculated I-I bong length of $I_2$ of 2.682 Å (Fig. S12) is consistent with the reported value [74,75]. As described in Fig. S13, we constructed adsorption models of $I_2$ molecule adsorbed at the metal sites and S sites

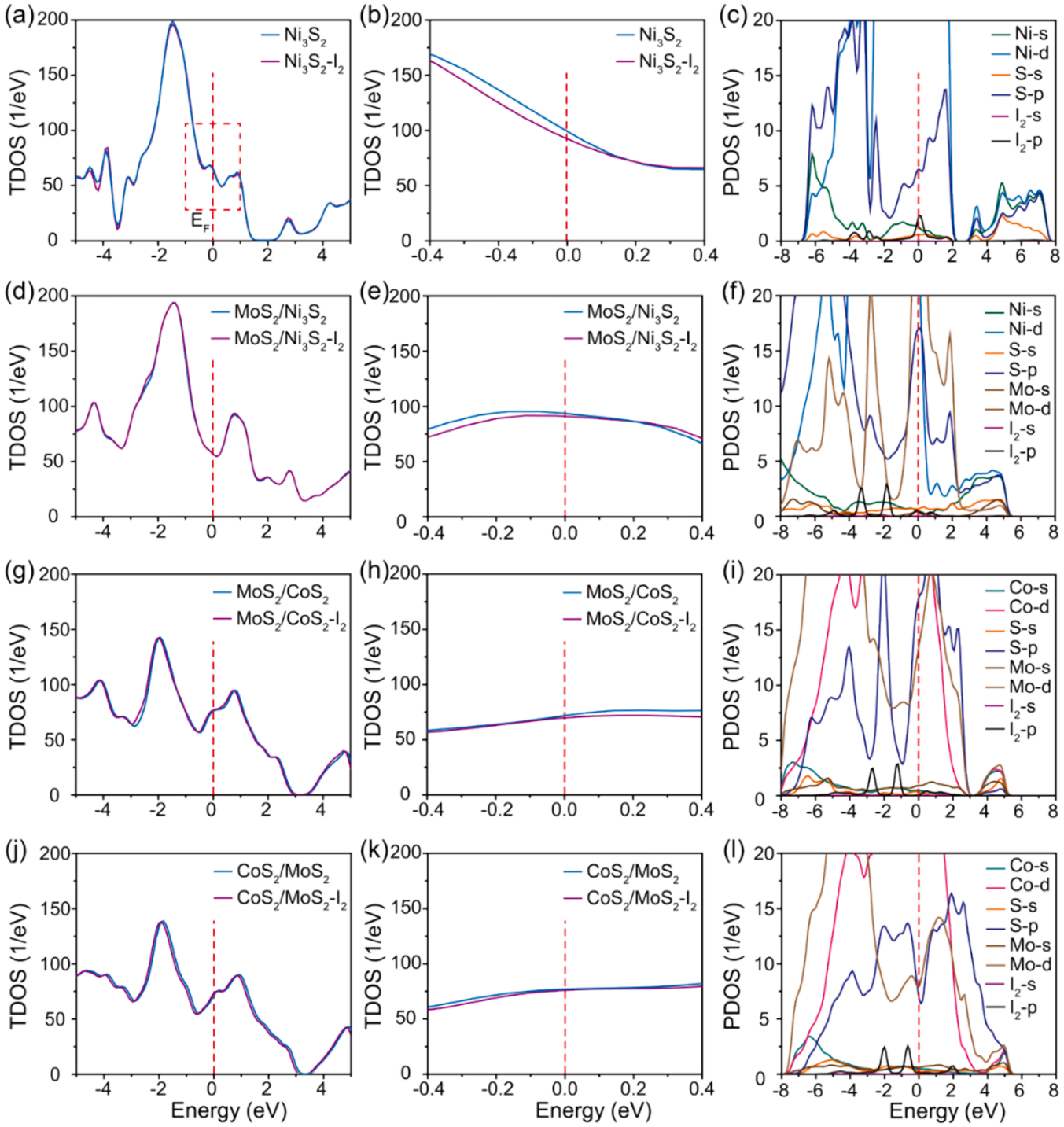


**Fig. 9.** The TDOS of (a, b) $Ni_3S_2$, (d, e) $MoS_2/Ni_3S_2$, (g, h) $MoS_2/CoS_2$ and (j, k) $CoS_2/MoS_2$ with and without adsorption $I_2$ molecules; PDOS of $I_2$ adsorption on (c) $Ni_3S_2$, (f) $MoS_2/Ni_3S_2$, (i) $MoS_2/CoS_2$ and (l) $CoS_2/MoS_2$.

of $Ni_3S_2$, $MoS_2/Ni_3S_2$, $MoS_2/CoS_2$ and $CoS_2/MoS_2$, respectively, and the optimized adsorption models are shown in Fig. 8. The corresponding $E_{ad}$ and equilibrium configuration parameters are summarized in Table S1. For $Ni_3S_2$, the $E_{ad}$ of $I_2$ molecule at Ni site (-3.76 eV) and S site (-2.61 eV) are both negative, indicating that the adsorption state of $I_2$ at all the sites of $Ni_3S_2$ is stable. Moreover, in the optimized adsorption model of $Ni_3S_2$ (Fig. 8a), the $I_2$ molecule is adsorbed at the center of three Ni atoms with the same length of Ni-I bond. Also, the Ni site shows the smaller $E_{ad}$ (-3.76 eV) and shorter Ni-I bond length (2.560 Å) than S site does (Table S1), demonstrating a stronger binding force between $I_2$ and Ni. In addition, compared with the I-I bond (2.682 Å) of the free $I_2$ molecule, the I-I bond (3.062 Å) of the $I_2$ molecule adsorbed at Ni site is significantly elongated compared with that at the S site (Fig. 8a,a'), suggesting that the $I_2$ adsorbed at the Ni site has stronger reactivity during adsorption. Notably, when we place $I_2$ at Mo and S sites of $MoS_2/Ni_3S_2$ and $MoS_2/CoS_2$, respectively (as shown in Fig. S13b and Fig. S13c), after structural optimization, we found the $I_2$ is eventually attached to the S sites (see Fig. 8b,b' and Fig. 8c,c'). This indicates that S is more conducive to the $I_2$ capture than Mo, that is, S atoms on the surface of $MoS_2/Ni_3S_2$ and $MoS_2/CoS_2$ are the favorable adsorption sites.

However, for $CoS_2/MoS_2$ (Fig. 8d,d', $CoS_2$ works as adsorption surface), $E_{ad}$ values at both Co and S sites are positive (Table S1), indicating that the adsorption of $I_2$ on the surface of $CoS_2/MoS_2$ is unfavorable, in other words, $CoS_2$ does not directly serve as sorption site in the adsorption of $I_2$.

The electronic structure contributes to a deeper understanding of the iodine capture mechanism. We know that iodine molecules are excellent electron acceptors, so the charge transfer between iodine and sorbents can effectively improve the adsorption property [29,35]. As shown in Fig. S14, the peak intensity of total density of states (TDOS) of $MoS_2/Ni_3S_2$, $MoS_2/CoS_2$ and $CoS_2/MoS_2$ at the Fermi level are larger than that of $Ni_3S_2$, meaning higher carrier density. This facilitates electron transfer, resulting in higher activity at the interface than the single phase of $Ni_3S_2$. In Fig. 9a,b, compared with $Ni_3S_2$, the TDOS of $Ni_3S_2$-I is reduced at the Fermi level, which may be due to the charge transfer from the $Ni_3S_2$ to $I_2$. As well known, the hybridization between atomic orbitals can be observed by analyzing the overlap of the orbital peaks on the PDOS curve, which further indicates the strength of the interatomic interactions [76]. In the projected density of states (PDOS) of $Ni_3S_2$-I (Fig. 9c), the peaks of $I_2$-p, Ni-s, Ni-d, S-s and S-p orbitals are observed to be hybridization at the Fermi level, demonstrating a strong interaction between $I_2$ and Ni/S that changes the electronic structure of $Ni_3S_2$. After iodine adsorption, the TDOS of $MoS_2/Ni_3S_2$-I decreases at Fermi level (Fig. 9d,e), indicating that there exists electron transfer between $MoS_2/Ni_3S_2$ interface and $I_2$. Moreover, the PDOS of $MoS_2/Ni_3S_2$-I shows a small overlap between $I_2$ orbital and $MoS_2/Ni_3S_2$ at Fermi level (Fig. 9f), which may result from the interaction between $I_2$ and $Ni_3S_2$ at the interface of $MoS_2/Ni_3S_2$. For the $MoS_2/CoS_2$ ($MoS_2$ as the adsorption surface), after the adsorption of iodine, the TDOS of $MoS_2/CoS_2$-I drops slightly at the Fermi level (Fig. 9g,h), and there is no hybridized between $I_2$-p orbital and $MoS_2/CoS_2$ observed in the PDOS of $MoS_2/CoS_2$-I (Fig. 9i). Combined with the above adsorption energy data that the $E_{ad}$ of $I_2$ at S sites on the surface of $MoS_2/CoS_2$ are negative, the $MoS_2/CoS_2$ may rely on the electrostatic adsorption to trap iodine, and do not covalently bond with I. However, the peak intensity of TDOS of $CoS_2/MoS_2$ ($CoS_2$ as adsorption surface) is unchanged at Fermi level before and after iodine trapping (Fig. 9j,k), implying that the iodine adsorption does not affect the electronic structure of $CoS_2/MoS_2$. Furthermore, the PDOS of $CoS_2/MoS_2$-I shows that the $I_2$-p orbital is far away from the Fermi level (Fig. 9l), further demonstrating that there is no direct interaction between $I_2$ and $CoS_2$. These results suggest that $CoS_2$ does not act as the adsorption site. Combined with XPS and XAFS results, the contribution of $CoS_2$ to $I_2$ capture may originate from the electron transfer of Co → Mo and Co → Ni, which enhances the reactivity of $MoS_2$ and $Ni_3S_2$ at the interfaces.

To sum up, iodine capture mechanism of $MoS_2/CoS_2/Ni_3S_2$/NF is summarized as follows: (1) the morphology of nanorods wrapped with fluffy nanosheets of $MoS_2/CoS_2/Ni_3S_2$/NF provides more adsorption sites for $I_2$ capture; (2) the sulfides as soft Lewis bases possess a strong affinity for $I_2$ with soft Lewis acidic nature, facilitating the capture of a large amounts of iodine; (3) $Ni_3S_2$/NF component plays a leading role in chemical sorption of $I_2$ forming $NiI_2$ and $S_8$; (4) $MoS_2$ makes an important contribution to iodine capture mainly through electrostatic adsorption; (5) for $CoS_2$, REDOX potential of $Co^{2+}/Co^{3+}$ and interfacial electron transfers of Co → Mo and Co → Ni significantly promote the iodine sorption capability via synergistic interactions.

## 4. Conclusions

In summary, a series of $MoS_2/CoS_2/Ni_3S_2$/NF composites are fabricated via one-step hydrothermal reaction to achieve excellent iodine capture. The optimal $MoS_2/CoS_2/Ni_3S_2$/NF-13 owns the most favorable morphology of nanorods coated with fluffy nanosheets, providing more adsorption sites to endow an extremely large iodine adsorption capacity of 1804 mg/g. According to HSAB theory, the $MoS_2/CoS_2/Ni_3S_2$/NF composites possess high affinity for Lewis soft acidic $I_2$, which is conducive to the capture of large amount of $I_2$. For $Ni_3S_2$/NF, both $S^{2-}$ and $Ni^0$ reduce $I_2$ molecules to $I^-$ ions, and the $Ni^{2+}$ ions combine with $I^-$ forming $NiI_2$. The calculated $E_{ad}$ and PDOS *via* DFT demonstrate stronger interactions between $I_2$ and $Ni_3S_2$, suggesting the REDOX reaction. For the $MoS_2$, the iodine capture is mainly via electrostatic adsorption. Though $CoS_2$ does not adsorb $I_2$ directly, it promotes the iodine capture through electron transfers of Co → Mo and Co → Ni. The interactions including HSAB, REDOX, electrostatic attraction, as well as electron transfer, all belong to chemical adsorptions, which contribute to the wonderful capture capacity of iodine. This work provides a novel idea for designing new and high-efficiency metal sulfides-based iodine sorbents.

## CRediT authorship contribution statement

**Chaonan Wang:** Writing – review & editing, Writing – original draft, Methodology, Investigation, Conceptualization. **Huiqin Yao:** Project administration, Funding acquisition. **Jingtong Sun:** Validation, Methodology, Investigation. **Tian Tong:** Data curation, Formal analysis. **Zi Ye:** Methodology, Investigation. **Hongliang Dong:** Validation, Methodology, Investigation. **Cheng Li:** Validation, Project administration, Methodology. **Shulan Ma:** Writing – review & editing, Supervision, Funding acquisition, Conceptualization.

## Declaration of competing interest

The authors declare that they have no known competing financial interests or personal relationships that could have appeared to influence the work reported in this paper.

## Data availability

Data will be made available on request.

## Acknowledgements

This work is supported by the National Science Foundation of China (No. 22176017) and Natural Science Foundation of Ningxia (2023AAC02039). Shanghai Key Laboratory of Material Frontiers Research in Extreme Environments (MFree), China (No. 22dz2260800) and Shanghai Science and Technology Committee, China (No. 22JC1410300). We also thank the 1W2B beamline station at Beijing Synchrotron Radiation Facility (BSRF), the BL17B station of National Facility for Protein Science in Shanghai (NFPS) and BL13SSW station at Shanghai Synchrotron Radiation Facility (SSRF) for the help in characterizations.

## Appendix A. Supplementary data

Supplementary data to this article can be found online at https://doi.org/10.1016/j.cej.2024.152514.

## References

[1] H. Zhu, C. Yu, B. Wang, W. Zhu, T. Duan, Y. Wei, G. He, D. Sun, J. Zhou, Sponge-inspired reassembly of 3D hydrolyzed collagen aerogel with polyphenol-functionalization for ultra-capturing iodine from airborne effluents, Chem. Eng. J. 428 (2022) 131322.

[2] Y. Yin, Y. Yang, G. Liu, H. Chen, D. Gong, Y. Ying, J. Fan, S. Liu, Z. Li, C. Wang, Z. Guo, Z. Li, C. Yu, G. Zeng, Ultrafast solid-phase synthesis of 2D pyrene-alkadiyne frameworks towards efficient capture of radioactive iodine, Chem. Eng. J. 441 (2022) 135996.

[3] B. Tian, R. Zhang, H. Liu, X. Xu, Q. Chen, J. Hu, Z. Chen, Turning waste into wealth: Efficient and reversible iodine capture by decoration of coordinative allylic moiety to a flexible covalent organic framework and its application for catalysis, Sep. Purif. Technol. 330 (2024) 125459.

[4] T. Na, H. Zhu, P. Chen, F. Liu, Y. Yi, J. Zhou, T. Duan, J. Lei, In-situ growth nanoscale zero-valent bismuth 3D honeycomb-like material for highly efficient

selective capture of iodine vapor in complex environments, Sep. Purif. Technol. 330 (2024) 125421.
[5] X. Chen, L. Wang, C. Ding, H. Xie, H. Zou, J. Deng, Z. Liu, J. Shi, Y. Ding, Highly efficient removal of radioactive iodine anions by nano silver modified activated carbon fiber, Appl. Surf. Sci. 643 (2024) 158644.
[6] B.J. Riley, S. Chong, J. Schmid, J. Marcial, E.T. Nienhuis, M.K. Bera, S. Lee, N. L. Canfield, S. Kim, M.A. Derewinski, R.K. Motkuri, Role of zeolite structural properties toward iodine capture: a head-to-head evaluation of framework type and chemical composition, ACS Appl. Mater. Interfaces 14 (2022) 18439–18452.
[7] W. Zhou, A. Li, M. Zhou, Y. Xu, Y. Zhang, Q. He, Nonporous amorphous superadsorbents for highly effective and selective adsorption of iodine in water, Nat. Commun. 14 (2023) 538.
[8] Z. Zheng, Q. Lin, L. Xie, X. Chen, H. Zhou, K. Lin, D. Zhang, X. Chi, J.L. Sessler, H. Wang, Macrocycle polymeric networks based on a chair-like calix[4]pyrrole for the rapid and efficient adsorption of iodine from water, J. Mater. Chem. A 11 (2023) 13399–13408.
[9] Y. Lu, Z. Yu, T. Zhang, D. Pan, J. Dai, Q. Li, Z. Tao, X. Xiao, A cucurbit[8]uril-based supramolecular framework material for reversible iodine capture in the vapor phase and solution, Small (2023) 2308175.
[10] X. Liu, H. Yuan, Q. Zheng, B. Huang, F. Liao, H. Gao, H. Fu, J. Zhang, Y. Liao, Understanding the adsorption sites on nitrogen- and oxygen-doped carbon nanotubes for iodine uptake, Appl. Surf. Sci. 629 (2023) 157387.
[11] L. Liu, L. Chen, K. Thummavichai, Z. Ye, Y. Wang, T. Fujita, X. Wang, Amino-functionalized MOF-on-MOF architectural nanocomplexes composed for radioactive-iodine efficient adsorption, Chem. Eng. J. 474 (2023) 14585.
[12] X. He, L. Chen, X. Xiao, Y. Gan, J. Yu, J. Luo, H. Dan, Y. Wang, Y. Ding, T. Duan, Improved utilization of $Cu^0$ for efficient adsorption of iodine in gas and solution by mesoporous $Cu^0$-SBA-15 via solvothermal reduction method, Chem. Eng. J. 462 (2023) 142175.
[13] Y. Wu, Y. Guo, R. Su, X. Ma, Q. Wu, Z. Zeng, L. Li, X. Yao, S. Wang, Hierarchical porous carbon with an ultrahigh surface area for high-efficient iodine capture: insights into adsorption mechanisms through experiments, simulations and modeling, Sep. Purif. Technol. 303 (2022) 122237.
[14] Y. Xie, T. Pan, Q. Lei, C. Chen, X. Dong, Y. Yuan, W.A. Maksoud, L. Zhao, L. Cavallo, I. Pinnau, Y. Han, Efficient and simultaneous capture of iodine and methyl iodide achieved by a covalent organic framework, Nat. Commun. 13 (2022) 2878.
[15] Y. Gao, Y. Huo, M. Chen, X. Su, J. Zhan, L. Wang, F. Liu, J. Zhu, Y. Zeng, J. Fan, Z. Li, R. Chen, H.L. Wang, Phenolic based porous carbon fibers with superior surface area and adsorption efficiency for radioactive protection, Adv. Fiber Mater. 5 (2023) 1431–1446.
[16] Y. Feng, L.H. Wu, C.H. Zhang, B.X. Zhou, S.R. Zheng, W.G. Zhang, S.L. Cai, J. Fan, Porous amorphous metal-organic frameworks based on heterotopic triangular ligands for iodine and high-capacity dye adsorption, Dalton Trans. 52 (2023) 12087–12097.
[17] B. Wang, H. Zhu, T. Duan, G. He, Y. Wei, J. Zhou, Multi-layer active interface construction with polyphenols and nano-silver on nano collagen fiber for efficient capturing iodine vapor, Appl. Surf. Sci. 596 (2022) 153585.
[18] A. Bo, S. Sarina, Z. Zheng, D. Yang, H. Liu, H. Zhu, Removal of radioactive iodine from water using $Ag_2O$ grafted titanate nanolamina as efficient adsorbent, J. Hazard. Mater. 246–247 (2013) 199–205.
[19] X.H. Pan, M.J. Jin, J.H. Zu, G. Han, J.J. Diao, S.Y. Liu, Q. Tang, Efficient removal of radioactive iodide from contaminated seawater by radiation-resistant $Ag^+$-doping polypropylene nonwoven adsorbents, Sep. Purif. Technol. 345 (2024) 127287.
[20] J. Zhang, N. Pu, M. Li, W. Sang, Q. He, Q. Tian, W. Zhang, High-efficient Ag(I) ion binding, Ag(0) nanoparticle loading, and iodine trapping in ultrastable benzimidazole-linked polymers, Sep. Purif. Technol. 328 (2024) 125052.
[21] L. Chen, J.Y. Qian, D.D. Zhu, S. Yang, J. Lin, M.Y. He, Z.H. Zhang, Q. Chen, Mesoporous zeolitic imidazolate framework-67 nanocrystals on siliceous mesocellular foams for capturing radioactive iodine, ACS Appl. Nano Mater. 3 (2020) 5390–5398.
[22] T. Pan, X. Dong, Y. Han, Efficient capture of iodine and methyl iodide using all-silica EMM-17 zeolite, Nano Res. 16 (2023) 6308–6315.
[23] B. Zheng, X. Liu, J. Hu, F. Wang, X. Hu, Y. Zhu, X. Lv, J. Du, D. Xiao, Construction of hydrophobic interface on natural biomaterials for higher efficient and reversible radioactive iodine adsorption in water, J. Hazard. Mater. 368 (2019) 81–89.
[24] S.M. Scott, T. Hu, T. Yao, G. Xin, J. Lian, Graphene-based sorbents for iodine-129 capture and sequestration, Carbon 90 (2015) 1–8.
[25] K.S. Subrahmanyam, D. Sarma, C.D. Malliakas, K. Polychronopoulou, B.J. Riley, D. A. Pierce, J. Chun, M.G. Kanatzidis, Chalcogenide aerogels as sorbents for radioactive iodine, Chem. Mater. 27 (2015) 2619–2626.
[26] K.S. Subrahmanyam, C.D. Malliakas, D. Sarma, G.S. Armatas, J. Wu, M. G. Kanatzidis, Ion-exchangeable molybdenum sulfide porous chalcogel: gas adsorption and capture of iodine and mercury, J. Am. Chem. Soc. 137 (2015) 13943–13948.
[27] L. Wang, T. Li, X. Dong, M. Pang, S. Xiao, W. Zhang, Thiophene-based MOFs for iodine capture: effect of pore structures and interaction mechanism, Chem. Eng. J. 425 (2021) 130578.
[28] P. Chen, X. He, M. Pang, X. Dong, S. Zhao, W. Zhang, Iodine capture using Zr-based metal-organic frameworks (Zr-MOFs): adsorption performance and mechanism, ACS Appl. Mater. Interfaces 12 (2020) 20429–20439.
[29] J. Li, H. Zhang, L. Zhang, K. Wang, Z. Wang, G. Liu, Y. Zhao, Y. Zeng, Two-dimensional covalent-organic frameworks for ultrahigh iodine capture, J. Mater. Chem. A 8 (2020) 9523–9527.
[30] Y. Zhu, Y. Qi, X. Guo, M. Zhang, Z. Jia, C. Xia, N. Liu, C. Bai, L. Ma, Q. Wang, A crystalline covalent organic framework embedded with a crystalline supramolecular organic framework for efficient iodine capture, J. Mater. Chem. A 9 (2021) 16961–16966.
[31] J. Wang, D. Fan, C. Jiang, L. Lu, Host-guest interaction-mediated nanointerface engineering for radioiodine capture, Nano Today 36 (2021) 101034.
[32] X. Li, X. Wang, L. Dong, Q. Zou, C. He, Y. Zhu, T. Fujita, C. Liao, C.W. Kao, Y.R. Lu, Combining electrospinning and hydrothermal methods to prepare $Bi_2S_3$@$SiO_2$ nanostructure-based membranes for enhanced capture capacity of off-gas Iodine from a nuclear plant, ACS Appl. Nano Mater. 6 (2023) 4328–4336.
[33] C.N. Wang, H.Q. Yao, Z.D. Cai, S.K. Han, K.R. Shi, Z.L. Wu, S.L. Ma, $[Sn_2S_6]^{4-}$ anion-intercalated layered double hydroxides for highly efficient capture of iodine, ACS Appl. Mater. Interfaces 15 (2023) 52496–52505.
[34] C.N. Wang, C. Miao, S.K. Han, H.Q. Yao, Q.Q. Zhong, S.L. Ma, Highly efficient capture of iodine vapor by $[Mo_3S_{13}]^{2-}$ intercalated layered double hydroxides, J. Colloid Interface Sci. 659 (2024) 550–559.
[35] Y.R. Lee, X.H. Do, K.Y. Cho, K. Jeong, K.Y. Baek, Amine-functionalized zeolitic imidazolate framework-8 (ZIF-8) nanocrystals for adsorption of radioactive iodine, ACS Appl. Nano Mater. 3 (2020) 9852–9861.
[36] Z. Zhang, Q. Zhao, M. Huang, X. Ouyang, Adsorption of hazardous gases in nuclear islands on monolayer $MoS_2$ sheet, Adsorption 25 (2019) 159–171.
[37] N.S. Komarov, T.V. Pavlova, B.V. Andryushechkin, Iodine adsorption on Ni(110): 2D-phase transitions and $NiI_2$ growth, J. Phys. Chem. C 123 (2019) 27659–27665.
[38] B. Qiao, H. Yan, C. Wang, H. Yao, Z. Cai, K. Shi, R. Liu, S. Ma, $Ni_xS_y$/NF composites assembled by sulfidation of nickel foam (NF) for highly effective capture of iodine, Chem. Eng. J. 479 (2024) 147864.
[39] K. Wu, Y.L. Huang, J. Zheng, D. Luo, M. Xie, Y.Y. Li, W. Lu, D. Li, A microporous shp-topology metal-organic framework with an unprecedented high-nuclearity $Co_{10}$-cluster for iodine capture and histidine detection, Mater. Chem. Front 5 (2021) 4300–4309.
[40] Y. Lin, P. Zeng, D. Wang, T.T. Li, L.H. Wu, S.R. Zheng, A mixed-ligand Co(II) MOF synthesized from a single organic ligand to capture iodine and methyl iodide vapour, Dalton Trans. 52 (2023) 7709–7717.
[41] Y. Yang, H. Yao, Z. Yu, S.M. Islam, H. He, M. Yuan, Y. Yue, K. Xu, W. Hao, G. Sun, H. Li, S. Ma, P. Zapol, M.G. Kanatzidis, Hierarchical nanoassembly of $MoS_2$/$Co_9S_8$/$Ni_3S_2$/Ni as a highly efficient electrocatalyst for overall water splitting in a wide pH range, J. Am. Chem. Soc. 141 (2019) 10417–10430.
[42] W. Kohn, L.J. Sham, Self-consistent equations including exchange and correlation effects, Phys. Rev. 140 (1965) 1133–1138.
[43] P.E. Blochl, Projector augmented-wave method, Phys. Rev. B 50 (1994) 17953–17979.
[44] G. Kresse, J. Furthmuller, Efficient iterative schemes for ab initio total-energy calculations using a plane-wave basis set, Phys. Rev. 54 (1996) 11169–11186.
[45] J.P. Perdew, K. Burke, M. Ernzerhof, Generalized gradient approximation made simple, Phys. Rev. Lett. 77 (1996) 3865–3868.
[46] W. Xie, K. Liu, G. Shi, X. Fu, X. Chen, Z. Fan, M. Liu, M. Yuan, M. Wang, $CoS_2$ nanowires supported graphdiyne for highly efficient hydrogen evolution reaction, J. Energy Chem. 60 (2021) 272–278.
[47] C.K. Tang, X. Zheng, X.L. Chen, Y.G. Fu, Q.F. Lü, Defect-rich $MoS_2$/$CoS_2$ on $Mo_2TiC_2T_x$ MXene as an efficient catalyst for hydrogen evolution reaction in acidic media, FlatChem 42 (2023) 100581.
[48] C. Wang, Z. Yu, H. Yao, R. Jin, K. Shi, Y. Li, S. Ma, Triangular nanosheet arrays of O-doped Co/Fe disulfides as highly efficient electrocatalysts for the hydrogen evolution reaction, J. Alloy. Compd. 964 (2023) 171257.
[49] Q. Wang, L. Yan, L. Wang, W. Zhang, Y. Guo, W. Song, X. Li, Enhanced peroxymonosulfate activation by $(NH_4)_2Mo_3S_{13}$ for organic pollutant removal: Crucial roles of adsorption and singlet oxygen, J. Environ. Chem. Eng. 10 (2022) 107966.
[50] L.X. Yang, L.X. Xie, M.L. Chu, H. Wang, M.W. Yuan, Z.H. Yu, C.N. Wang, H.Q. Yao, S.M. Islam, K.R. Shi, D.P. Yan, S.L. Ma, M.G. Kanatzidis, $Mo_3S_{13}^{2-}$ intercalated layered double hydroxide: Highly selective removal of heavy metals and simultaneous reduction of $Ag^+$ ions to metallic $Ag^0$ ribbons, Angew. Chem. Int. Ed. 134 (2022) 202112511.
[51] V. Pundir, A. Gaur, R. Kaur, V.B. Aashi, Nano-interfacial interactions in 2-D $Ni_3S_2$-$Ni_3N$ nanosheets for the hydrogen evolution reaction in an alkaline medium, Energy Adv. 2 (2023) 321–327.
[52] R. Sun, Z.H. Su, Z.F. Zhao, M.Q. Yang, T.S. Li, J.X. Zhao, Y.C. Shang, $Ni_3S_2$ nanocrystals in-situ grown on Ni foam as highly efficient electrocatalysts for alkaline hydrogen evolution, Rare Met. 42 (2023) 3420–3429.
[53] P. Kuang, T. Tong, K. Fan, J. Yu, In situ fabrication of Ni-Mo bimetal sulfide hybrid as an efficient electrocatalyst for hydrogen evolution over a wide pH range, ACS Catal. 7 (2017) 6179–6187.
[54] Q. Zhang, T. Yao, Q. He, H. Wang, Z. Liu, D. Wang, H. Wang, L. Meng, Enhancing lithium-ion storage performance of hollow $CoS_2$/$MoS_2$ nanospheres via N-doped carbon-coating, J. Energy Storage 72 (2023) 108639.
[55] J. Yang, C. Chai, C. Jiang, L. Liu, J. Xi, $MoS_2$-$CoS_2$ heteronanosheet arrays coated on porous carbon microtube textile for overall water splitting, J. Power Sources 514 (2021) 230580.
[56] T.L.L. Doan, D.C. Nguyen, K. Kang, A. Ponnusamy, H.I. Eya, N.Y. Dzade, C.S. Kim, C.H. Park, Advanced Mott-Schottky heterojunction of semi-conductive $MoS_2$ nanoparticles/metallic $CoS_2$ nanotubes as an efficient multifunctional catalyst for urea-water electrolysis, Appl. Catal. B-Environ. 342 (2024) 123295.
[57] M. Jiang, L. Zhu, Q. Zhao, G. Chen, Z. Wang, J. Zhang, L. Zhang, J. Lei, T. Duan, Novel synthesis of NaY-NH4F-$Bi_2S_3$ composite for enhancing iodine capture, Chem. Eng. J. 443 (2022) 136477.
[58] T.D. Dinh, D. Zhang, V.N. Tuan, High iodine adsorption performances under off-gas conditions by bismuth-modified ZnAl-LDH layered double hydroxide, RSC Adv. 10 (2020) 14360–14367.

[59] Q. Zhao, L. Zhu, G. Lin, G. Chen, B. Liu, L. Zhang, T. Duan, J. Lei, Controllable synthesis of porous Cu-BTC@polymer composite beads for iodine capture, ACS Appl. Mater. Interfaces 11 (2019) 42635–42645.
[60] G. Lin, L. Zhu, T. Duan, L. Zhang, B. Liu, J. Lei, Efficient capture of iodine by a polysulfide-inserted inorganic NiTi-layered double hydroxides, Chem. Eng. J. 378 (2019) 122181.
[61] A. Yadav, S. Chong, B.J. Riley, J.S. McCloy, A. Goel, Iodine capture by Ag-loaded solid sorbents followed by Ag recycling and iodine immobilization: an end-to-end process, Ind. Eng. Chem. Res. 62 (2023) 3635–3646.
[62] X. Wang, M. Li, J. Zhang, X. He, J.C. Crittenden, W. Zhang, Silver ion-exchanged anionic metal-organic frameworks for iodine adsorption: silver species evolution from ions to nanoparticles, ACS Appl. Nano Mater. 6 (2023) 7206–7217.
[63] B.J. Riley, S. Chong, C.L. Beck, Iodine vapor reactions with pure metal wires at temperatures of 100–139 °C in air, Ind. Eng. Chem. Res. 60 (2021) 17162–17173.
[64] B.J. Riley, K. Carlson, Radioiodine sorbent selection criteria, Front. Chem. 10 (2022) 969303.
[65] T.G. Levitskaia, S. Chatterjee, B.W. Arey, E.L. Campbell, Y. Hong, L. Kovarik, J. M. Peterson, N.K. Pence, J. Romero, V. Shutthanandan, B. Schwenzer, T. Varga, RedOx-controlled sorption of iodine anions by hydrotalcite composites, RSC Adv. 6 (2016) 76042–76055.
[66] Y. Zhang, L. He, T. Pan, J. Xie, F. Wu, X. Dong, X. Wang, L. Chen, S. Gong, W. Liu, L. Kang, J. Chen, L. Chen, L. Chen, Y. Han, S. Wang, Superior iodine uptake capacity enabled by an open metal-sulfide framework composed of three types of active sites, CCS Chem. 5 (2023) 1540–1548.
[67] T. Bai, F. Wu, Y. Zhang, C. Mao, G. Wang, Y. Wu, H. Bai, Y. Li, Sulfur modification with dipentene and ethylhexyl acrylate to enhance asphalt mixture performance, Constr. Build. Mater. 343 (2022) 128086.
[68] L.R.L. Ting, Y. Deng, L. Ma, Y.J. Zhang, A.A. Peterson, B.S. Yeo, Catalytic activities of sulfur atoms in amorphous molybdenum sulfide for the electrochemical hydrogen evolution reaction, ACS Catal. 6 (2016) 861–867.
[69] C. Chang, L. Wang, L. Xie, W. Zhao, S. Liu, Z. Zhuang, S. Liu, J. Li, X. Liu, Q. Zhao, Amorphous molybdenum sulfide and its Mo-S motifs: Structural characteristics, synthetic strategies, and comprehensive applications, Nano Res. 15 (2022) 8613–8635.
[70] H. Liu, X. Wang, J. Wu, Y. Chen, J. Wan, R. Wen, J. Yang, Y. Liu, Z. Song, L. Xie, Vapor deposition of magnetic van der waals $NiI_2$ crystals, ACS Nano 14 (2020) 10544–10551.
[71] Y. Ding, W. Fan, Q. Xian, H. Dan, L. Zhu, T. Duan, Capture of iodine gas by $Bi^0$ modified silica with different morphologies: Influence of pore characteristic on the stable and unstable forms of adsorption, Chem. Eng. J. 451 (2023) 138887.
[72] Q. Xian, L. Chen, W. Fan, Y. Liu, X. He, H. Dan, L. Zhu, Y. Ding, T. Duan, Facile synthesis of novel $Bi^0$-SBA-15 adsorbents by an improved impregnation reduction method for highly efficient capture of iodine gas, J. Hazard. Mater. 424 (2022) 127678.
[73] M. Yuan, H. Yao, L. Xie, X. Liu, H. Wang, S.M. Islam, K. Shi, Z. Yu, G. Sun, H. Li, S. Ma, M.G. Kanatzidis, Polypyrrole-$Mo_3S_{13}$: an efficient sorbent for the capture of $Hg^{2+}$ and highly selective extraction of $Ag^+$ over $Cu^{2+}$, J. Am. Chem. Soc. 142 (2020) 1574–1583.
[74] K. Li, Y.L. Zhao, J. Deng, C.H. He, S.J. Ding, W.Q. Shi, Adsorption of radioiodine on $Cu_2O$ surfaces: a first-principles density functional study, Acta Phys. -Chim. Sin. 32 (2016) 2264–2270.
[75] T. Dayin, Z. Yaolin, W. Yuqi, H. Zitong, W. Jie, Z. Jun, Y. Chenxi, Theoretical investigation of volatile iodine adsorption onto COF-103, Chem. J. Chinese Universities 45 (2024) 20230401.
[76] Y. Gui, P. Luo, C. Ji, Y. Lin, X. Chen, First-principles study of the gas sensing of benzene and formaldehyde by $Ag_2O$- and CuO-modified $MoSe_2$ nanosheets, ACS Appl. Nano Mater. 5 (2022) 12907–12914.